PNAS RESEARCH ARTICLE | BIOPHYSICS AND COMPUTATIONAL BIOLOGY

Single-molecule force spectroscopy reveals intra- and intermolecular interactions of *Caenorhabditis elegans* HMP-1 during mechanotransduction

Shimin Le[a,b,1], Miao Yu[c,1], Chaoyu Fu[a,d,1], Jonathon A. Heier[e], Sterling Martin[f], Jeff Hardin[e,f,2], and Jie Yan[a,d,g,h,2]

Affiliations are included on p. 10.

Edited by Taekjip Ha, Children's Hospital Boston, Boston, MA; received January 31, 2024; accepted July 15, 2024

The *Caenorhabditis elegans* HMP-2/HMP-1 complex, akin to the mammalian β-catenin-α-catenin complex, serves as a critical mechanosensor at cell–cell adherens junctions, transducing tension between HMR-1 (also known as cadherin in mammals) and the actin cytoskeleton. Essential for embryonic development and tissue integrity in *C. elegans*, this complex experiences tension from both internal actomyosin contractility and external mechanical microenvironmental perturbations. While offering a valuable evolutionary comparison to its mammalian counterpart, the impact of tension on the mechanical stability of HMP-1 and HMP-2/HMP-1 interactions remains unexplored. In this study, we directly quantified the mechanical stability of full-length HMP-1 and its force-bearing modulation domains (M1-M3), as well as the HMP-2/HMP-1 interface. Notably, the M1 domain in HMP-1 exhibits significantly higher mechanical stability than its mammalian analog, attributable to interdomain interactions with M2-M3. Introducing salt bridge mutations in the M3 domain weakens the mechanical stability of the M1 domain. Moreover, the intermolecular HMP-2/HMP-1 interface surpasses its mammalian counterpart in mechanical stability, enabling it to support the mechanical activation of the autoinhibited M1 domain for mechanotransduction. Additionally, the phosphomimetic mutation Y69E in HMP-2 weakens the mechanical stability of the HMP-2/HMP-1 interface, compromising the force-transmission molecular linkage and its associated mechanosensing functions. Collectively, these findings provide mechanobiological insights into the *C. elegans* HMP-2/HMP-1 complex, highlighting the impact of salt bridges on mechanical stability in α-catenin and demonstrating the evolutionary conservation of the mechanical switch mechanism activating the HMP-1 modulation domain for protein binding at the single-molecule level.

HMP-1 | HMP-2 | salt bridges | magnetic tweezers

Cell-cell adhesions play crucial roles in embryonic development and tissue integrity. These adhesions are formed and regulated by a variety of force-bearing proteins that assemble into supramolecular physical linkages. Within these linkages, force-bearing proteins interact with numerous signaling proteins in a manner sensitive to mechanical cues, forming the physical basis for mechanotransduction (1). For instance, the classical cadherin-based adherens junction is linked to the actin cytoskeleton through a core complex, comprising a linear arrangement of cadherin, β-catenin, α-catenin, and F-actin. Molecular tension sensors have estimated the tension within this linkage to be on the order of several piconewtons (pN) (2–4). The mechanobiochemical regulation of the mammalian adherens junction has been intensively investigated in recent years (4–12). Signaling proteins interact with mechanosensing proteins in the complex in a force-dependent manner. For example, in mammals α-catenin recruits vinculin in a tension-dependent manner, which is hypothesized to regulate the strength of the adherens junction, and which converts mechanical cues into a cascade of downstream biochemical signaling events (5–13). Molecular modeling and Förster resonance energy transfer (FRET) assays suggest that salt bridges within the mammalian α-catenin M domain regulate the extensibility of α-catenin and its binding affinity for vinculin (9). However, this hypothesis has not been directly tested using single-molecule approaches.

The counterparts of the mammalian cadherin/catenin complex in *Caenorhabditis elegans* have served as an important model system for studying the role of the cadherin/catenin complex in living embryos, but remain less well understood (2–4). In *C. elegans*, the adherens junction is linked to the actin cytoskeleton through a core HMR-1(cadherin)-HMP-2(β-catenin)-HMP-1(α-catenin)-F-actin supramolecular

Significance

The authors show that the *Caenorhabditis elegans* HMP-2/HMP-1 complex, which mediates force transmission from adherens junctions to the actin cytoskeleton, has a long lifetime under physiological levels of tension, and that HMP-1 protein domains undergo reversible unfolding and refolding transitions in response to tension in the piconewton range. They present quantitative single-molecule mechanical assessment of interdomain interactions within the modulation domain (M1-3) of an α-catenin. These interactions strongly stabilize the M1 domain, regulating accessibility to force-dependent ligands and setting a high threshold of tension to activate mechanotransduction.

Author contributions: S.L., M.Y., J.H., and J.Y. designed research; S.L., M.Y., and C.F. performed research; J.A.H. and S.M. contributed new reagents/analytic tools; S.L., M.Y., and C.F. analyzed data; and S.L., C.F., J.A.H., J.H., and J.Y. wrote the paper.

The authors declare no competing interest.

This article is a PNAS Direct Submission.

[1] S.L., M.Y., and C.F. contributed equally to this work.

[2] To whom correspondence may be addressed. Email: jdhardin@wisc.edu or phyyj@nus.edu.sg.

This article contains supporting information online at https://www.pnas.org/lookup/suppl/doi:10.1073/pnas.2400654121/-/DCSupplemental.

Published September 5, 2024.

linkage, and capable of interacting with DEB-1 (vinculin) via its M1 domain(Fig. 1*A*) (14–21). The extracellular domains of HMR-1 interact with HMR-1 on neighboring cells to transmit forces across adjacent cells. The adherens junction is subject to tensile forces arising from both internal actomyosin contraction and external mechanical microenvironmental perturbations. It is widely believed to play crucial functions in mechanotransduction within cells and across tissues (15, 18, 22). However, how these core proteins respond to physiological levels of tension remains poorly understood. The mechanical stability of the protein–protein interfaces within this linkage, which determines the integrity of tension-transmission, has yet to be investigated. Moreover, it remains unclear whether the mechanobiochemical regulation of adherens junctions is evolutionarily conserved in nematodes.

In this study, we use single-molecule force spectroscopy to investigate the mechanobiochemical regulation of the HMP-1 protein, and the protein–protein interface it forms with HMP-2. Using magnetic tweezers for single-protein manipulation (23–25), we show that the force-bearing domains of HMP-1 unfold under pN scale tensions. Of particular interest and significance is the salt bridge-mediated interdomain interaction between M1 and M2-M3, which leads to stronger mechanical stabilization of the M1 domain in HMP-1. This stabilization significantly raises the tension threshold (to nearly 15 pN) necessary for mechanically exposing the cryptic vinculin binding site (VBS) within the M1 domain for high-affinity vinculin binding. This is in sharp contrast to mammalian α-catenins, where the cryptic VBSs are readily exposed at tensions slightly above 5 pN (5, 12). Furthermore, our results show that the HMP-2/HMP-1 interface has an average lifetime ranging from tens of seconds to tens of minutes within a physiologically relevant tension range. Finally, a phosphotyrosine-mimetic mutation (Y69E) in HMP-2 significantly weakens the mechanical stability of the HMP-2/HMP-1 interface. Together, these results reveal the intricate interplay between mechanical and biochemical regulation of HMR-1/HMP-2/HMP-1-mediated force transmission and the tension-dependent interactions of the core components of the *C. elegans* cadherin/catenin complex. This research provides deeper insights into the molecular mechanisms underlying mechanotransduction at the adherens junction of *C. elegans*. In particular, it represents quantitative single-molecule analysis of the role of salt bridges in mechanically stabilizing the M domain of an α-catenin.

Results

Mechanical Stability of Full-Length HMP-1. To investigate the mechanical stability of full-length HMP-1, we designed a single-molecule construct in which full-length HMP-1 is inserted between four well-characterized titin Ig 27 domains (I27, two repeats at each end) acting as a molecular spacer (26–28). The N- and C- termini of the construct feature a biotinylated AviTag and a SpyTag (27, 29), respectively, enabling specific tethering (Fig. 1*B*). Furthermore, we introduced a 572-bp DNA handle between the single-molecule construct and the superparamagnetic bead. This DNA handle acts as an additional spacer, preventing nonspecific interactions between the bead and the surface (27, 28, 30). A magnetic-tweezer setup was implemented to apply well-controlled force to the tethered molecule and record real-time changes in bead height (23–25). Due to force balance, this setup ensures that the tension within the molecule matches the applied force. More details on the single-molecule construct can be found in *SI Appendix*, Text S1.

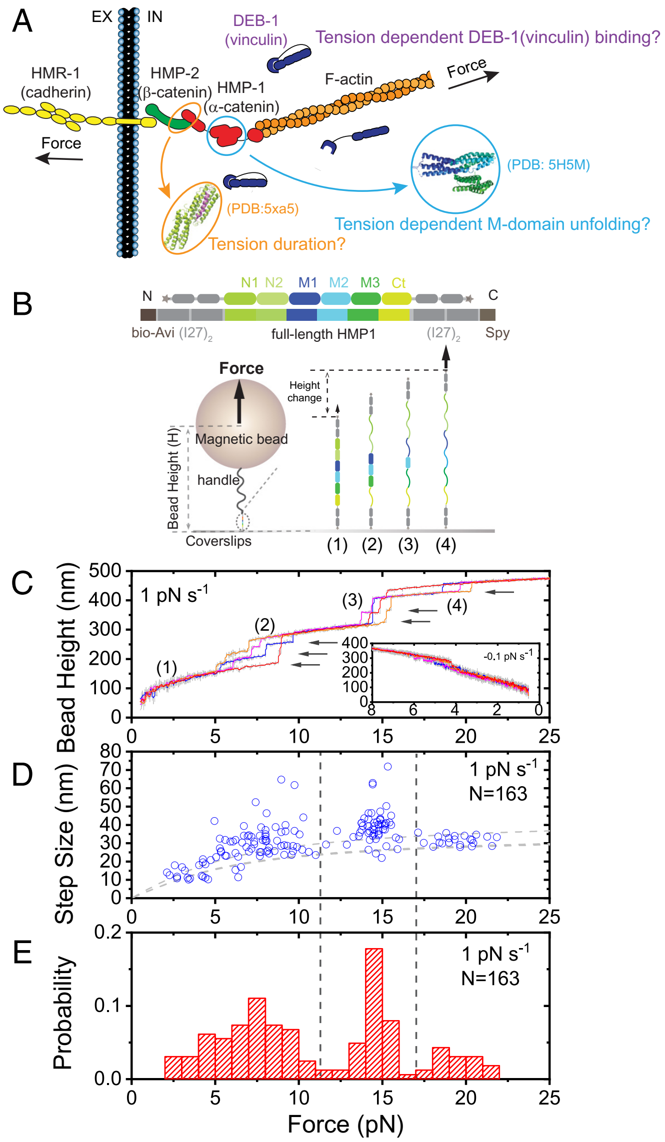

Fig. 1. Mechanical stability of full-length HMP-1. (*A*) Illustration of the force-transmission supramolecular linkage from membrane HMR-1 (cadherin) to the actin cytoskeleton via HMP-2 (β-catenin) and HMP-1 (α-catenin), DEB-1 (vinculin) in the surrounding solution, and questions raised related to the mechanotransduction mediated by this linkage. (*B*) Sketches of the single-molecule construct and the experimental design. The *Top* panel shows the domain map of the construct: AviTag, two repeats of I27 domain $(I27)_2$, full-length HMP-1, $(I27)_2$, SpyTag. The *Bottom* panel shows a single-molecule tether between a SpyCatcher-coated coverslip surface and a biotin-DNA-coated superparamagnetic bead (via streptavidin). Structural changes of the domains in the tether lead to extension changes of the molecule, which can be detected by the corresponding bead height changes. (*C*) Four representative force–height curves of a full-length HMP-1 tether during force-increase scans at a loading rate of 1 pN s^{-1}. The colored curves were obtained by 10-point FFT (fast Fourier transformation) smoothing of the raw data (gray). The arrows indicate the unfolding events of the six domains in HMP-1. The *Inset* shows the refolding events during force-decrease scans at a loading rate of −0.1 pN s^{-1}. (*D* and *E*) The resulting force-dependent unfolding step sizes and the normalized force histogram obtained over 30 repeats of scans from three independent tethers. N in panel (*D*) indicates the total number of unfolding events.

Fig. 1*C* shows the typical force-height curves of full-length HMP-1 during linear force-increase scans with a force-loading rate of 1 pN s^{-1}, ranging from ∼1 pN to 30 pN. Within each force-increase scan, six unfolding events were clearly observed, indicated by six step-wise bead height transitions (black arrows in Fig. 1*C*). These stepwise changes in bead height equal the extension change of the tethered molecule due to structural changes (23, 31). Notably, the I27 domain exhibits remarkable mechanical stability and unfolds at a slow rate of around 10^{-3} s^{-1} within the typical force range and room temperature conditions (26, 32). Consequently, these six unfolding events correspond to the unfolding of the six structured domains within full-length HMP-1, i.e., the two N-terminal domains (N1, and N2), three modulation domains (M1, M2, and M3), and the C-terminal F-actin binding domain. These unfolded domains have the capacity to refold at forces <6 pN during force-decrease scans (*Inset* of Fig. 1*C*, with a loading rate of −0.1 pN s^{-1}), allowing for repeated force scans through multiple cycles on a single tethered molecule.

Performing over 30 force-increase scans, we obtained the force-step size graph of the unfolding events (Fig. 1*D*) and the corresponding unfolding force distributions (Fig. 1*E*). It is evident that the mechanical unfolding of the six domains can be roughly categorized into three mechanical groups: Three domains unfold within a force range of 3 to 10 pN, two domains unfold at 10 to 15 pN, and one domain unfolds at 16 to 22 pN (*SI Appendix*, Fig. S1 *A*–*C*). In addition, occasionally, two domains unfolded concurrently (within our temporal resolution of 10 ms), as indicated by a single unfolding event associated with a step size that corresponds to the sum of the step sizes of two individual domains. The results from the mechanical unfolding of the full-length HMP-1 suggest that all the functional domains of HMP-1 respond to physiological levels of force (2–4).

Mechanical Stability of the Modulation Domains of HMP-1. As the modulation domains contain key binding sites for signaling proteins such as vinculin (19), we sought to probe the mechanical stability of the tension-bearing modulation domain of HMP-1. In a manner similar to the full-length HMP-1 construct, we prepared a single-molecule construct named "HMP-1-M123," which contains the three modulation domains (Fig. 2*A*). Fig. 2*B* shows the typical force-height curves for HMP-1-M123 during force-increase scans with a force loading rate of 1 pN s^{-1}, during which three unfolding events corresponding to the three modulation domains were observed. Repeating such force-increase scans over 100 times, we obtained a 2D graph displaying force-dependent step sizes (Fig. 2*C*) and the unfolding force distributions for the three modulation domains (Fig. 2*D*). Notably, two of the domains unfolded almost concurrently at forces in the range of 10 to 15 pN, whereas the third domain unfolded at a higher force of 15 to 20 pN (*SI Appendix*, Fig. S1 *D*–*F*). The nearly concurrent unfolding of the two domains suggests that the unfolding of one domain depends on the other, and such cooperativity suggests an interaction between the two domains. In our analysis, if the two domains unfolded within a timeframe shorter than 0.1 s, the unfolding is attributed as a single-step process with a large step size (*SI Appendix*, Text S2 and Fig. S2).

When compared to the unfolding signals obtained from full-length HMP-1 (Fig. 1), the unfolding of the modulation domains can be assigned to the second and third mechanical groups of full-length HMP-1. Hence, the two N-terminal domains (N1 and N2) and C-terminal domain of HMP-1 likely belong to the first mechanical group, unfolding within the range of 3 to 10 pN (with a loading rate of 1 pN s^{-1}). In conjunction with the results presented in subsequent sections, this allows us to attribute the cooperative unfolding events to M1 and another domain from M2 or M3, with the third unfolding event corresponding to M2 or M3. Additionally, based on the force-dependent step sizes

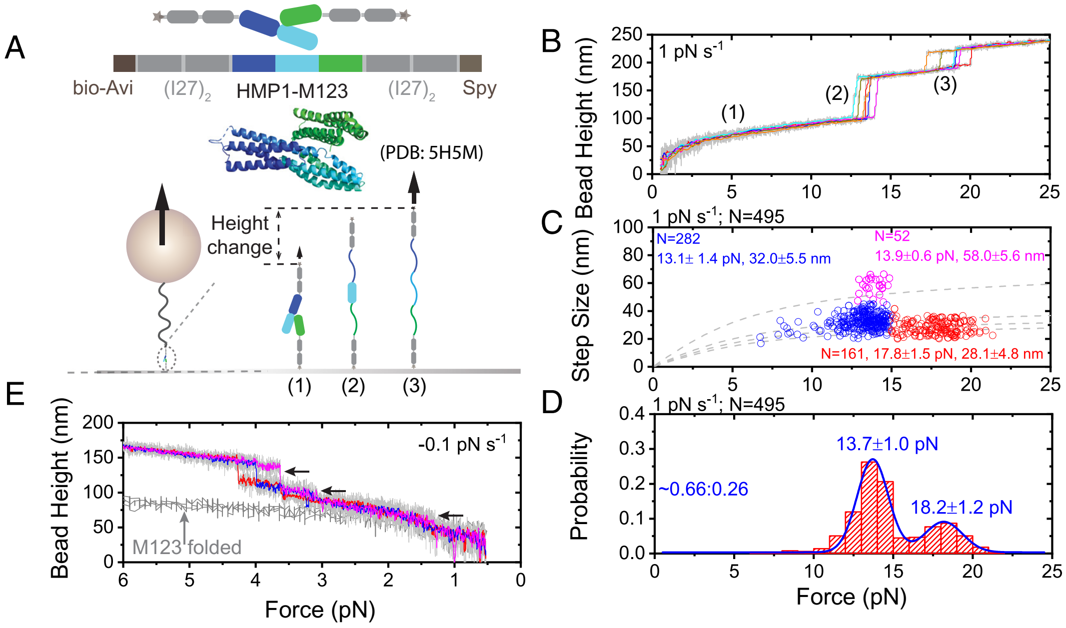

Fig. 2. Mechanical stability of the HMP-1 modulation domains. (*A*) Sketches of the single-molecule construct and the experimental design. The *Top* panel shows the domain map of the construct, and the structure of the modulation domains (PDB:5H5M) (19). The *Bottom* panel shows a single-molecule tether under force. (*B*) Five representative force–height curves of the HMP-1 modulation domains during force-increase scans at a loading rate of 1 pN s^{-1}. (*C* and *D*) The resulting force-dependent step sizes and the normalized force histogram of the unfolding events obtained over 165 repeats of scans from five tethers. The unfolding events are divided into three groups based on unfolding forces and step sizes. The data shown in magenta correspond to the unfolding of two domains within a timeframe shorter than 0.1 s, which is attributed as a single-step process with a large step size (*SI Appendix*, Text S2 and Fig. S2). The number of unfolding events (N) in each group and the corresponding average unfolding forces and step sizes are indicated (*C*). The blue curve in panel (*D*) is the double-Gaussian fitting to the normalized unfolding force histogram. The peak forces are indicated. The area ratio (0.66:0.26) of the two groups is also indicated. (*E*) Three representative force–height curves (colored curves) of HMP-1 modulation domains during force-decrease scans with a loading rate of −0.1 pN s^{-1} starting from a fully unfolded conformation. As a comparison, the force–height curves of the HMP-1 modulation domains with all three domains folded (gray curves) are also plotted.

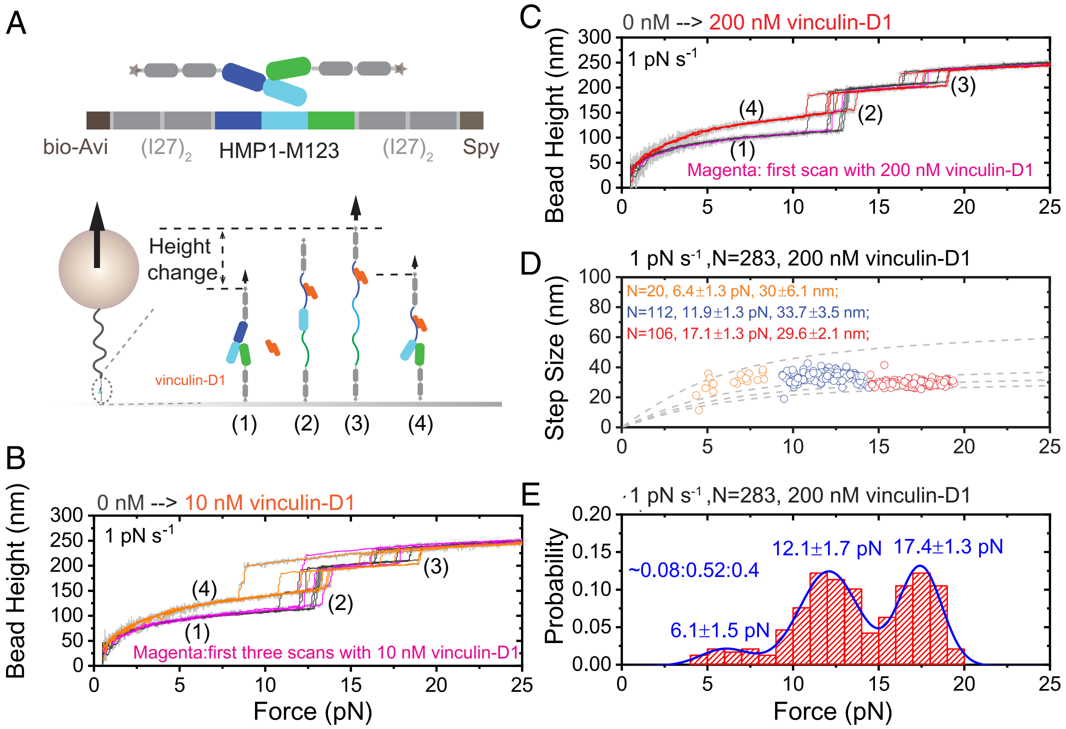

Fig. 3. Mechanical activation of HMP-1 modulation domains for vinculin-D1 binding. (*A*) The *Top* panel shows the domain map of the HMP-1 modulation domains. The *Bottom* panel shows a single-molecule tether under force. (*B*) Representative force-height curves during force-increase scans in the absence of vinculin-D1 (dark gray curves) and in the presence of 10 nM vinculin-D1 (magenta and orange curves). (*C*) Representative force-height curves during force-increase scans in the absence of vinculin-D1 (dark gray curves) and in the presence of 200 nM vinculin-D1 (magenta and red curves). (*D* and *E*) The resulting force-dependent step sizes and the normalized unfolding force histogram obtained over 150 repeats of scans from five tethers in 200 nM vinculin-D1. The unfolding events are divided into three groups based on unfolding forces. The number of unfolding events (N) in each group and the corresponding average unfolding forces and step sizes are indicated (*D*). The blue curve in panel (*E*) is the triple-Gaussian fitting to the normalized unfolding force histogram. The peak forces and the area ratio (0.08:0.52:0.40) of the three groups are indicated.

of the third unfolding event, the contour length released in the third unfolding event is consistent with the unfolding of M2 but not M3 (*SI Appendix*, Text S3). Hence, we attribute the third unfolding event to M2 unfolding, and the preceding cooperative unfolding to M1-M3 co-unfolding. During force-decrease scans at forces of ~4 pN, 3 pN, and below 2 pN, respectively, the three unfolded modulation domains could refold in a stepwise manner, at a force loading rate of −0.1 pN s^{-1} (Fig. 2*E*).

Mechanical Activation of HMP-1 Modulation Domains. Similar to mammalian α-catenin, there is a single conserved VBS buried inside the HMP-1-M1 domain, which has been shown to bind to DEB-1 (the vinculin counterpart in *C. elegans*), as well as mammalian vinculin (19). Previous isothermal titration calorimetry (ITC) experiments have shown that the D1 domain of vinculin exhibits a low affinity for binding to the HMP-1-M123 domain. Specifically, vinculin-D1 binding was associated with a high dissociation constant (K_d) of ~600 nM (19). On the other hand, both D1 domains showed a significantly higher affinity for binding to the HMP-1-M1 domain alone, with K_d of ~3 nM for vinculin-D1 (19). These results suggest that the interdomain interaction between M1 and M23 greatly suppresses the binding of the D1 domain of vinculin to the VBS in the HMP-1-M1 domain. Given that the HMP-1 modulation domain is part of a tension transmission supramolecular linkage, it is reasonable to postulate that tension-induced disruption of the M1–M23 interaction could release the autoinhibitory interdomain interaction, thereby facilitating high-affinity binding of vinculin to HMP-1-M1.

We used the vinculin-D1 domain to test the hypothesized force-dependent activation of the M1 domain (Fig. 3*A* and *SI Appendix*, Fig. S3*A*). We first stretched the single-molecule HMP-1-M123 construct with multiple linear force-increase scans (at 1 pN s^{-1}) followed by force-decrease scans (at −0.1 pN s^{-1}). During this process, we observed the characteristic cooperative unfolding of two modulation domains, specifically M1 and M3, occurring at 10 to 15 pN, and the unfolding of the remaining modulation domain, M2, at 15 to 20 pN (Fig. 3*B*, dark gray curves). Additionally, we noted the characteristic refolding of these domains at lower forces (<5 pN) as depicted in Fig. 2*E*. We then introduced 10 nM vinculin-D1 (the vinculin-D1 domain, known to bind to the VBS in M1) at low forces of ~1 pN (ensuring that the domains remained folded during the solution exchange). We repeated the force-increase scans (Fig. 3*B*, magenta and orange curves). During several initial force-increase scans, the characteristic unfolding signals of the three M domains were still observed (magenta curves), followed by loss of the unfolding signature in one of the domains at 10 to 15 pN (orange curve in Fig. 3*B* and red curve Fig. 3*C*).

The observation of vinculin-D1 binding at 10 nM under force sharply contrasts with the K_d of ~600 nM measured between vinculin-D1 and HMP-1-M12 in the absence of force. It is, however, comparable to the binding between vinculin-D1 and mammalian αE-catenin when the latter is in the "open" conformation (33). This observation therefore aligns with the hypothesis that the force-induced unfolding of the HMP-1 modulation domains exposes the buried VBS, resulting in high-affinity binding to vinculin-D1. Subsequently, this high-affinity vinculin-D1 binding suppresses the refolding of the M1 domain during force-decrease scans.

At a higher concentration (200 nM) of vinculin-D1, we observed vinculin-D1 binding after the unfolding of the M domains during the initial force-increase scan. This indicates faster binding at the higher concentration (Fig. 3*C*). Fig. 3 *D* and *E* display the resulting force-dependent step sizes and transition forces for the remaining M2 and M3 domain unfolding events in the presence of 200 nM vinculin-D1 in solution. The unfolding force histogram reveals two major mechanical groups distributed over force ranges of 10 to 15 pN and 15 to 20 pN, respectively (*SI Appendix*, Fig. S1 *G–I*). Compared to the unfolding force distribution in the absence of vinculin-D1 (Fig. 2 *C* and *D*), the refolding of HMP-1-M1 is suppressed by vinculin-D1 binding, while the refolding and unfolding characteristics of HMP-1-M2 and HMP-1-M3 remain largely unaffected. Compared to the three refolded steps in the force-decrease scans at a force loading rate of −0.1 pN s^{-1} in Fig. 2*E*), only two unfolded modulation domains could refold in the presence of 200 nM vinculin-D1 (*SI Appendix*, Fig. S3*B*), further supporting the inference that vinculin binding suppresses refolding of the M1 domain. There is also a minor mechanical group with unfolding forces below 10 pN, spreading from 2.5 pN to 10 pN and lacking a clear centered peak, which might be attributed to altered refolding of the modulation domains due to vinculin-D1 binding (Fig. 3*E* and *SI Appendix*, Fig. S1 *G–I*).

In mammals, it is well established that vinculin-D1 binding to the VBS induces an α-helical structure in the VBS peptide. This structural transformation is associated with a force-dependent extension that differs from its randomly coiled conformation (5, 12, 27).This suggests that applied force can modulate the dynamics of vinculin-D1 binding and unbinding to the VBS. Notably, when a force in the range of 27 to 30 pN was applied to HMP-1 in the presence of 200 nM vinculin-D1, dynamic transitions between two distinct extension levels were observed, differing by ∼4 nm (*SI Appendix*, Fig. S3 *C* and *D*). Importantly, this 4 nm extension difference aligns with the expected difference between the α-helical and randomly coiled conformations of the VBS peptide under this force range (5, 12, 27). Given that forces significantly exceeding 20 pN are unlikely to be physiologically relevant (as detailed in *SI Appendix*, Text S4), the results suggest that the force-dependent dissociation of the HMP-1 VBS and vinculin-D1 complex occurs under forces applied to HMP-1 that exceed the scope of physiological relevance.

Salt Bridge Mutations in the HMP-1 M3 Domain Weaken the Mechanical Stability of the HMP-1 M1 Domain. Unexpectedly, the M1 domain of HMP-1 exhibits substantially greater mechanical stability compared to its mammalian counterparts, in which rapid unfolding of the M1 domain occurs at forces slightly above ∼5 pN under similar force-loading rates (5, 12). This significantly enhanced mechanical stability of the HMP-1 M1 domain suggests that it may result from either a higher intrinsic mechanical stability of the M1 domain or mechanical stabilization facilitated by interactions with neighboring domains. Our findings strongly support the latter, as the isolated M1 domain unfolds at forces below 5 pN when subjected to the same force-loading rate (*SI Appendix*, Fig. S4).

While it is believed that salt bridges play a crucial role in stabilizing the M domain through interactions between HMP-1-M1 and HMP-1-M2-M3 (19), their impacts on the mechanical stability, namely the unfolding forces during a force-loading process, of the M domains remain unexplored. For example, a salt bridge forms between Arg^{551} in M3 and Asp^{386} in M1, resulting in polar interactions with charged residues in neighboring bundles, thereby connecting M1, M2, and M3. This connection serves to stabilize the overall domain structure (19). Another salt bridge forms between Arg^{554} in M3 and Asp^{497} in M2, also playing a role in stabilizing a compact conformation of the M domain (19). To explore the effects of these salt bridges on the mechanical stability of the M domains, we introduced specific mutations, R551A and R554A, into the M3 domain to disrupt the interactions between HMP-1-M1 and HMP-1-M2-M3 (Fig. 4*A* and *SI Appendix*, Fig. S5).

Our results revealed that, following the introduction of the M3 mutations, the cooperative unfolding event disappeared, while the third unfolding step, potentially originating from the M2 domain, remained unchanged (Fig. 4*B*). Specifically, throughout repeated force cycles, we consistently observed an unfolding signal resembling M2 at 17.9 ± 2.7 pN with a step size of 27.4 ± 3.2 nm. However, the unfolding of the other two domains was not consistently observed in all cycles (*SI Appendix*, Fig. S6 *A* and *B*). In approximately 15% of the cycles, we noted a large step at a force of 11.6 ± 2.2 pN and a step size of 36.7 ± 6.5 nm, which matched the anticipated unfolding behavior of M3, particularly regarding step size. In less than 10% of the cycles, we observed unfolding at forces of 8.3 ± 3.0 pN and a step size of 15.8 ± 6.4 nm, which could be attributed to the unfolding of the M1 domain (Fig. 4 *C* and *D*). Consistent with this possibility, the introduction of a 200 nM vinculin-D1 solution led to the cessation of this unfolding event (Fig. 4 *E–G* and *SI Appendix*, Fig. S6 *C* and *D*).

In summary, our data strongly indicate that the removal of salt bridges abolishes the unfolding cooperativity between M1 and M3, significantly diminishing the mechanical stability of the M1 domain, which houses the cryptic VBS.

The HMP-2/HMP-1 Interface Provides Sufficient Mechanical Stability for Supporting Mechanotransduction. We have shown that the tension-induced rapid unfolding of the HMP-1 modulation domains involves forces in the range of 10 to 15 pN. To activate the trans-binding of signaling proteins in a tension-dependent manner, it is essential that the supramolecular linkage—HMR-1/HMP-2/HMP-1/F-actin—responsible for tension transmission can withstand this force range for a sufficient lifetime to facilitate tension-dependent interactions. Since the integrity of the tension-transmission pathway is dependent on the mechanical stability of protein–protein interfaces, it is important to measure the mechanical stability of these interfaces in the adherens junction complex. The HMP-2/HMP-1 interface is a critical protein–protein interface in the linkage, which comprises the N-terminal tail peptide of HMP-2 (Nt) and the N-terminal domain of HMP-1 (N12) (Fig. 5*A*) (20). We therefore sought to quantify the mechanical stability of this interface.

We employed a single-molecule construct designed to convert a protein–protein interaction into an intramolecular interaction (Fig. 5*A*) (10, 11, 27, 34–36). Briefly, the construct contains the HMP-2/HMP-1 interface, consisting of the N12 domain of HMP-1, the Nt peptide of HMP-2, and a long flexible unstructured peptide linker positioned in between. This construct is flanked by two repeats of I27 domains on each side. To enable specific tethering, an AviTag and a SpyTag are fused at each end of the construct (Fig. 5*A* and *SI Appendix*, Text S1). Under sufficiently low forces, N12 and Nt can interact with each other, effectively reconstituting the HMP-2/HMP-1 interface, and in the process, looping the extended linker. Conversely, when subjected to a sufficiently high force, the interface becomes

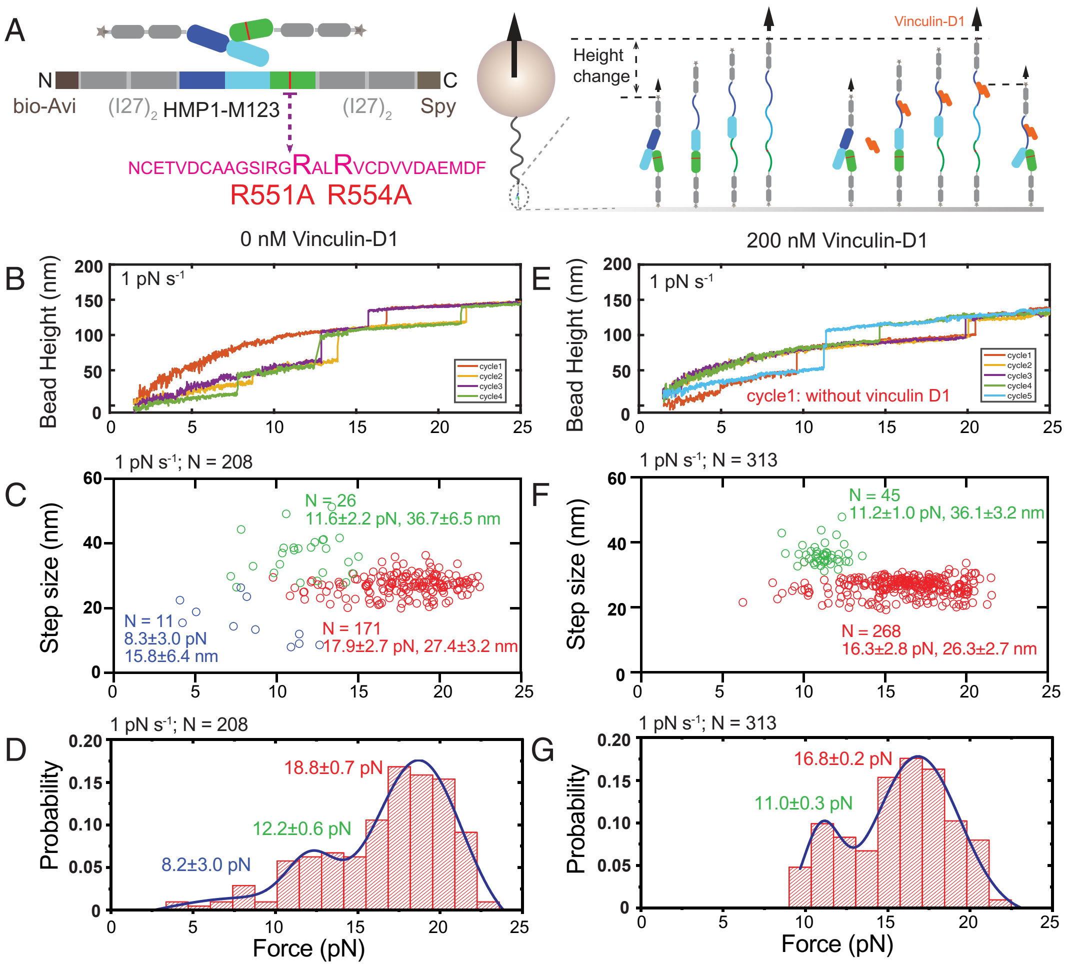

Fig. 4. Effects of R551A and R554A mutations in M3 on mechanical stability of the HMP-1 modulation domains. (*A*) The *Left* panel shows the domain map of the HMP-1 modulation domains with salt bridge mutations. The *Right* panel shows a schematic of the conformations of HMP1-M1-M2-M3 under force with or without vinculin D1. (*B*) Four representative force-height curves of the HMP-1 modulation domains carrying the R551A and R554A mutations in M3 during force-increase scans at a loading rate of 1 pN s^{-1}. (*C* and *D*) The resulting force-dependent step sizes and the normalized force histogram of the unfolding events obtained over 171 repeats of scans from 13 tethers. The unfolding events are divided into three groups indicated with different colors based on unfolding forces and step sizes. The number of unfolding events (N) in each group and the corresponding average unfolding forces and step sizes are indicated (*C*). The blue curve in panel (*D*) is the triple-Gaussian fitting to the normalized unfolding force histogram. The peak forces are indicated. (*E*) Representative force-height curves during force-increase scans in the absence of vinculin-D1 (cycle 1) and in the presence of 200 nM vinculin-D1 (cycle 2 to 5). Compared to panel (*B*), the unfolding events at forces below 10 pN were no longer observed for this tether during repeating force cycles. (*F* and *G*) The resulting force-dependent step sizes and the normalized unfolding force histogram obtained over 268 repeats of scans from 10 tethers in 200 nM vinculin-D1. Compared to panels (*C* and *D*), the weakest group corresponding to unfolding events at forces below 10 pN disappears. The number of unfolding events (N) in each group and the corresponding average unfolding forces and step sizes are indicated (*F*). The blue curve in panel (*G*) is the double-Gaussian fitting to the normalized unfolding force histogram.

destabilized, resulting in the rupture of the interaction and the subsequent release of the extended linker. This rupture event leads to a sudden extension increase in the construct, as evidenced by a distinctive stepwise increase in bead height, equivalent to the extension increase (31).

Fig. 5*B* shows typical force-height curves of the HMP-2/HMP-1 interface construct during force-increase scans with a loading rate of 1 pN s^{-1}. Clearly, in each scan, a single bead height jump of 110.9 ± 8.4 nm (N = 178) was consistently observed at 16.6 ± 1.7 pN (N = 178). The size of the bead height increases at these forces is consistent with the extension of the linker and unfolding of the N12 domain, suggesting concurrent rupturing of the interface and the unfolding of the N12 domain. Similar force-increase scans were repeated over 50 times at three different force-loading rates: 0.2 pN s^{-1}, 1 pN s^{-1}, and 5 pN s^{-1}. The resulting force-dependent step sizes of the rupturing events are shown in Fig. 5*C*. The normalized histograms of rupturing forces at the three loading rates show that the interface ruptures at 15.9 ± 1.9 pN (N = 56), 16.6 ± 1.7 pN (N = 178), and 19.1 ± 3.1 pN (N = 106), respectively (Fig. 5*D*). These forces are greater than the unfolding forces of the first and second modulation domains at the corresponding loading rates, suggesting that the HMP-2/HMP-1 interface provides sufficient mechanical stability to support the mechanotransduction of the HMP-1 modulation domains. This is essential for the mechanical destabilization of the M1 domain, which is required for high-affinity vinculin binding.

To directly quantify the tension-dependent lifetime of the HMP-2/HMP-1 interface, we implemented a force-clamp assay. Briefly, the construct was initially held at a force of ~0.5 pN for 30 s to allow the formation of the interface. Subsequently, it was held at a target force in the range of 12 to 16 pN, and the dwell time until interface rupture was recorded. This procedure was repeated for multiple cycles (N > 50), and the average lifetime of the interface at this force was obtained by exponential fitting to the histogram of the dwell times (*Materials and Methods*). The force-dependent lifetimes of the interface

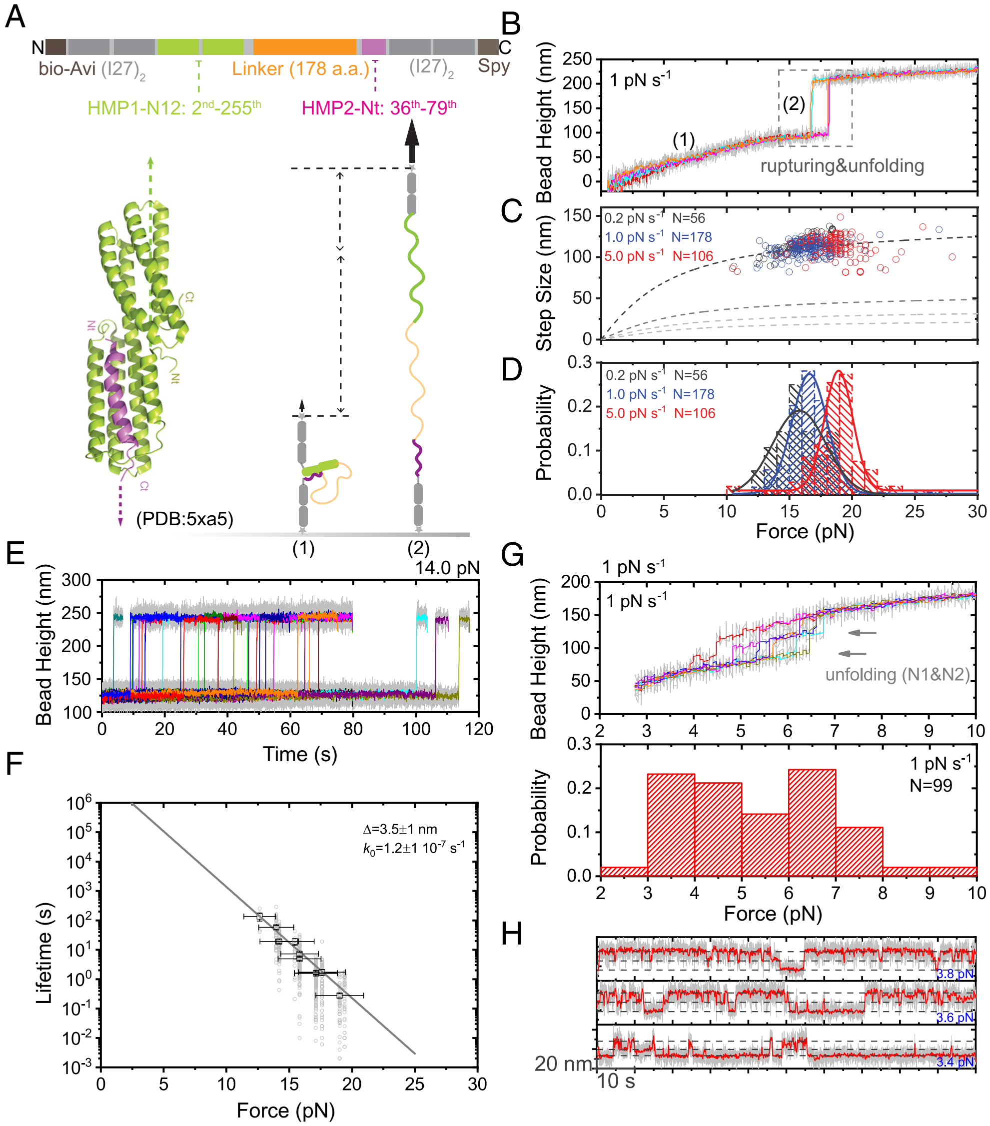

Fig. 5. Mechanical stability of the HMP-2/HMP-1 interface. (*A*) The single-molecule construct, the domain map, the structure of the HMP-2/HMP-1 interface (PDB:5XA5) (20), and the single-molecule tether under force. (*B*) Representative force–height curves of a tether during force-increase scans at a loading rate of 1 pN s^{-1}. (*C* and *D*) The resulting force-dependent step sizes (*C*) and the normalized rupturing force histograms (*D*) obtained over 50 repeats of scans for five tethers at three indicated force loading rates. The number of rupturing events, the average forces, and the average step sizes at corresponding loading rates are N = 56, $F = 15.9 \pm 1.9$ pN, $\Delta H = 115.4 \pm 12.2$ nm (0.2 pN s^{-1}); N = 178, $F = 16.6 \pm 1.7$ pN, $\Delta H = 110.9 \pm 8.4$ nm (1 pN s^{-1}); and N = 106, $F = 19.1 \pm 3.1$ pN, $\Delta H = 112.6 \pm 14.2$ nm (5 pN s^{-1}). (*E*) Representative force–height curves of a tether during force-clamp at 14.0 pN. The stepwise bead height jumps indicate the rupturing of the HMP-2/HMP-1 interface. (*F*) The resulting force-dependent average lifetime $\tau(F)$ of the HMP-2/HMP-1 interface obtained from such force-clamp experiments, which can be well fitted with Bell's model, $\tau(F) = k_0^{-1} e^{\frac{-F\Delta}{k_B T}}$, where Δ is the transition distance and k_0 is the extrapolated zero-force rupturing rate. (*G*) *Top*: representative force–height curves of the tether during force-increase scans at the indicated loading rate starting from a conformation in which the HMP-2/HMP-1 interface was not re-formed, whereas the N1 and N2 domains were refolded. *Bottom*: the resulting normalized unfolding force histogram during the force-increase scans. (*H*) Representative time traces of the bead height at indicated constant forces, before the re-formation of the interface. Dynamic unfolding and refolding of the N1 and N2 domains were observed.

were obtained by performing such measurements at different targeting forces (Fig. 5 *E* and *F*). Notably, the force-dependent lifetime consistently indicates that the HMP-2/HMP-1 interface possesses greater mechanical stability than the M1 domain. For instance, at a force of ∼14 pN, the HMP-2/HMP-1 interface can persist for tens of seconds, while the M1 domain unfolds almost instantaneously under the same force.

In addition, the construct also enabled us to quantify the mechanical responses of the N12 domains of HMP-1. Consistent with the data from full-length HMP-1 unfolding experiments, the N1 and N2 domains unfolded at forces ranging from 3 to 9 pN during force-increase scans at a loading rate of 1 pN s^{-1} (Fig. 5*G*). The equilibrium unfolding/refolding dynamics of the N1 and N2 domains can be observed at constant forces around 4 pN (Fig. 5*H*). Interestingly, when HMP-2's N-terminal peptide is bound to the N12 domain, the unfolding of N12 occurs concurrently with the dissociation of the HMP-2/HMP-1 interface at significantly higher forces of ∼16 pN. This suggests that the binding of HMP-1's N-terminal peptide stabilizes the N12 domain against mechanical unfolding. This phenomenon is also observed in the stabilization of mouse α-catenin's N12 domain by the N-terminal peptide from β-catenin (10), and in the stabilization of mouse vinculin's D1 domain by talin's and α-catenin's VBS peptide (11).

Single-Residue Phosphorylation-Mimetic Mutations in HMP-2 Weaken the Mechanical Stability of the HMP-2/HMP-1 Interface. The N terminus of HMP-2 contains two phosphorylation residues, i.e., the 69th tyrosine (Y69) and the 47th serine (S47). These residues are situated within the HMP-2/HMP-1 interface. It was previously observed that introducing a Y69E or S47E mutation in HMP-2 disrupted cell–cell adhesion (20). This observation suggests that phosphorylation at these residues could weaken the stability of the HMP-2/HMP-1 interface, a hypothesis yet to be experimentally tested (20). We therefore aimed to quantify the effects of these mutations on the mechanical stability of the HMP-2/HMP-1 interface. To achieve this, we prepared two single-molecule constructs of the HMP-2/HMP-1 interface that carry 1) the Y69E mutation, or 2) the S47E mutation (Fig. 6*A*).

Fig. 6*B* shows typical force-height curves for the HMP-2/HMP-1$^{\mathrm{Y69E}}$ interface construct during force-increase scans at a loading rate of 1 pN s^{-1}. To explore this further, we conducted similar scans at three different force-loading rates (0.2 pN s^{-1}, 1 pN s^{-1}, and 5 pN s^{-1}). We obtained the resulting force-dependent step sizes of interface rupturing (corresponding to the first stepwise bead height increase) and domain unfolding transitions (Fig. 6*C*), and the corresponding interface rupturing force distributions for these three force-loading rates (Fig. 6*D*). Interestingly, we observed a two-peak distribution in the interface rupturing force, which was separated by performing k-mean clustering on the force-step size plot (*SI Appendix*, Fig. S7 *A*–*C*). For instance, at 1 pN s^{-1} one peak occurred at 14.1 ± 1.4 pN (N =184) and another at 6.1 ± 2.1 pN (N = 90), which is in sharp contrast to the single-peaked rupturing force distribution (peak force at 16.6 ± 1.7 pN for 1 pN s^{-1}, Fig. 5) observed in the wild-type interface. Similar experiments performed on the HMP-2/HMP-1$^{\mathrm{S47E}}$ interface resulted in a single-peak distribution (peak force at 14.7 ± 1.5 pN, N = 261), slightly lower than the wild-type interface peak force (Fig. 6 *E*–*G*). These results demonstrate that the phosphorylation of one or two of the residues leads to decreased mechanical stability of the HMP-2/HMP-1 interface. Notably, the Y69E mutation appears to have a more pronounced weakening effect on the mechanical stability of the interface. Consistent with this interpretation, the lifetimes of the HMP-2/HMP-1$^{\mathrm{Y69E}}$ interface were within 200 s at forces of 1 to 2 pN, whereas the HMP-2/HMP-1$^{\mathrm{S47E}}$ interface remained stable over thousands of seconds, even at a slightly higher force of ∼3 pN (*SI Appendix*, Fig. S8 *A* and *B*).

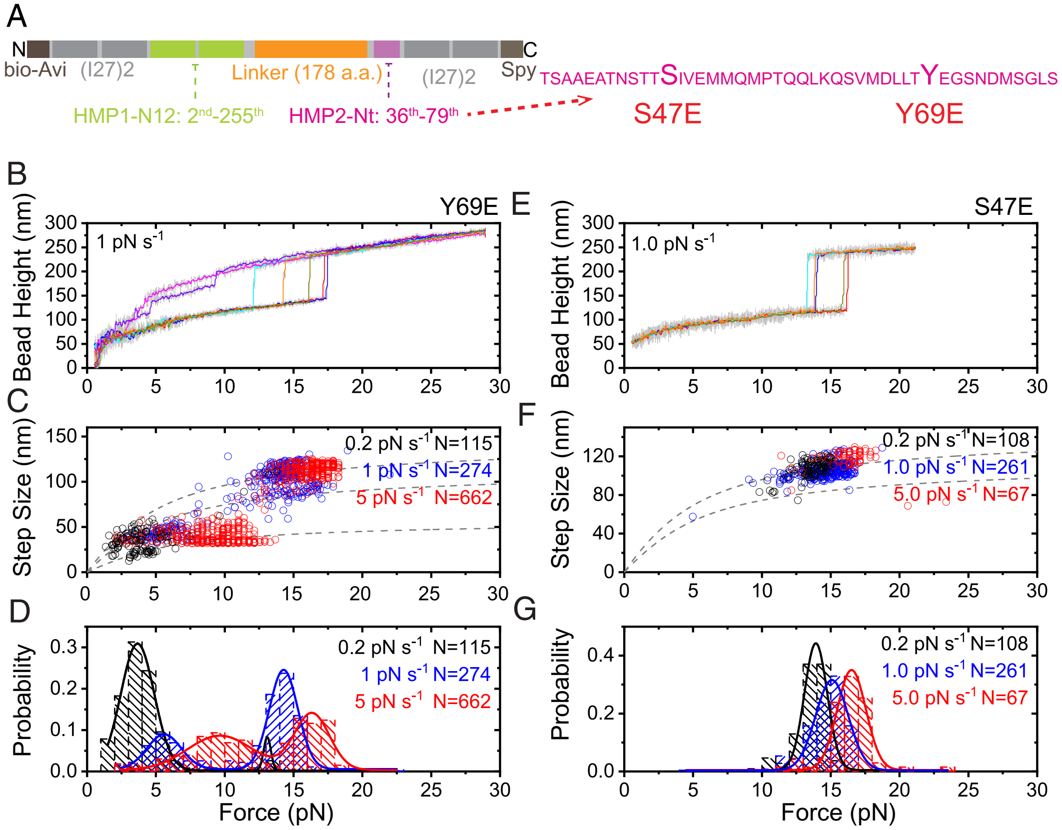

Fig. 6. Effects of Y69E or S47E mutations in HMP-2 on mechanical stability of the HMP-2/HMP-1 interface. (*A*) Sketches of the domain map and sequences of HMP-2-Nt. (*B*) Representative force–height curves of a HMP-1–HMP-2$^{\mathrm{Y69E}}$ interface tether during force-increase scans at 1 pN s^{-1}. (*C* and *D*) The resulting force-dependent step sizes and the normalized rupturing force histograms obtained at the three indicated loading rates. The number of rupturing events, the average forces, and the average step sizes at corresponding loading rates are N = 110, F = 3.8 ± 1.3 pN, ΔH = 33.6 ± 10.9 nm; N = 5, F = 13.0 ± 1.0 pN, ΔH = 106.1 ± 9.7 nm (0.2 pN s^{-1}, two groups); N = 90, F = 6.1 ± 2.1 pN, ΔH = 45.0 ± 9.4 nm; N = 184, F = 14.1 ± 1.4 pN, ΔH = 106.9 ± 12.5 nm (1.0 pN s^{-1}, two groups); N = 344, F = 8.9 ± 2.7 pN, ΔH = 39.7 ± 7.6 nm; and N = 318, F = 16.0 ± 1.4 pN, ΔH = 111.8 ± 9.1 nm (5.0 pN s^{-1}, two groups); (*E*) Representative force–height curves of a HMP-2/HMP-1$^{\mathrm{S47E}}$ interface tether during force-increase scans at 1 pN s^{-1}. (*F* and *G*) The resulting force-dependent step sizes and the normalized rupturing force histograms obtained at the three indicated loading rates. The number of rupturing events, the average forces, and the average step sizes at corresponding loading rates are N = 108, F = 13.6 ± 1.2 pN, ΔH = 107.4 ± 9.2 nm (0.2 pN s^{-1}); N = 261, F = 14.7 ± 1.5 pN, ΔH = 105.1 ± 7.9 nm (1.0 pN s^{-1}); N = 67, F = 16.3 ± 1.7 pN, ΔH = 117.3 ± 10.9 nm (5.0 pN s^{-1}).

Discussion

The M domain of α-catenin and the binding interface between β- and α-catenin are crucial for mechanotransduction mediated by the cadherin–catenin complex. In this study, we aimed to provide insights into the molecular mechanisms underlying the mechanobiochemical aspects of cell–cell adhesions mediated by HMP-2/HMP-1 in *C. elegans*. Our investigation was carried out systematically, focusing on the following: 1) Evaluating the mechanical stability of full-length HMP-1 protein, with a particular focus on the HMP-1 modulation domains under physiologically relevant loading; 2) Investigating the force-dependent activation of the HMP-1 M1 domain for exposure of vinculin binding site (Fig. 7); 3) Examining the impacts of inter-subdomain interactions within the M domain on the mechanical stability of M1; and 4) Assessing the mechanical stability of the HMP-2/HMP-1 interface, including its dependence on the phosphorylation of specific HMP-2 residues within the interface (*SI Appendix*, Text S5).

Our results revealed that the domains within HMP-1 can undergo unfolding when exposed to physiological levels of force, which are less than 20 pN. Importantly, our findings showed that the mechanical unfolding of the M1 subdomain is necessary for the exposure of the VBS for binding by vinculin's D1 domain. The force-induced exposure of the VBS for high-affinity vinculin binding has also been observed in other force-bearing mechanosensing proteins, such as talin and α-actinin (5, 27). Therefore, it appears that force-activated revealing of cryptic binding sites is a conserved strategy utilized by cells across different organisms. Intriguingly, SRGP-1, a GTPase-activating protein that stabilizes the cadherin-dependent adherens junction in *C. elegans*, has been reported to bind to a closed conformation of the M domain (37). Therefore, the force-dependent unfolding of the M domain may lead to a switch of binding partners, as depicted in Fig. 7.

An intriguing finding is that, despite the high degree of structural and domain organizational similarities between HMP-1 and its mammalian counterparts, we observed significant differences in the mechanical stability of the modulation domains. Notably, the force required to unfold the critical VBS-bearing M1 domain is ~5 pN for mammalian α-catenins compared to ~13 pN for HMP-1. This reveals a significantly greater level of autoinhibition for M1 unfolding in the case of HMP-1. This autoinhibition arises from the interdomain interaction between M1 and M2-M3.

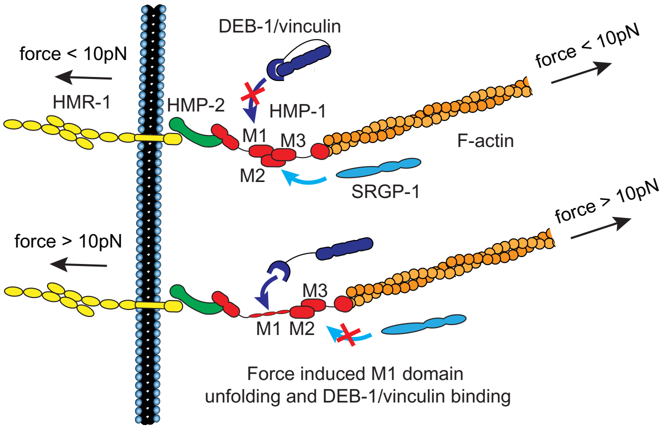

Fig. 7. Illustration the mechanotransduction of force-transmission supramolecular linkage from membrane HMR-1 (cadherin) to the actin cytoskeleton via HMP-2 (β-catenin) and HMP-1 (α-catenin). At low tensions, the M domain of HMP-1 assumes a compact conformation, where the SRGP-1 binds. At higher tensions, the M domain is extended and the M1 subdomain is unfolded. The mechanically unfolded M1 exposes the DEB-1 (vinculin) binding site.

The primary inter-subdomain interactions within the M domain are mediated by salt bridges. Previous work showed that salt bridge-disrupting mutations make HMP-1 much more susceptible to proteolysis (37). In the case of human α-catenin, it has also been observed that the M3 bundle plays a crucial role in stabilizing the M domain, thereby suppressing vinculin binding, as revealed in an ITC experiment (33). Moreover, the salt bridge mutant R551A in the M3 domain of mammalian α-catenin significantly enhances vinculin binding, as demonstrated in a pull-down assay (38). Consistent with this result, a previous biochemical assay showed that the elimination of these salt bridges increases the apparent binding affinity of the vinculin head domain nearly tenfold, from approximately 1.8 μM to 0.14 μM, indicating that inter-subdomain interactions significantly suppress vinculin binding (9).

Notably, these experiments were conducted without subjecting the M domain to physiological level of mechanical stretching. Thus, they do not offer direct insights into whether the bridges play a key role in enhancing the mechanical stability, rather than the thermal stability, of the M domain. Insights along this direction were obtained from full-atom molecular dynamics simulation studies (9, 39), which showed that salt bridges mediate inter-subdomain interactions within the mouse/human α-catenin M domain. These inter-subdomain interactions are suppressed by forces around 100 pN, which is substantially higher than the physiologically relevant forces ranging from a few pNs to tens of pNs (5, 40–42) due to the time scale limitations of full-atom molecular dynamics simulations. Critical insights have also been obtained from live cell studies, showing that salt-bridge disruption in the mouse/human α-catenin M domain increases dynamic vinculin recruitment to adherens junctions and the population of unfurled α-catenin (9). However, the key question regarding the impact of salt bridges on the mechanical stability of M1, which houses the vinculin binding site, has not been directly addressed quantitatively until now.

Our study addresses these gaps by demonstrating that the introduction of salt bridge mutants in the M3 domain of HMP-1 substantially reduces the mechanical stability of the M1 domain, leading to a lower mechanical activation threshold for vinculin binding. Furthermore, the introduction of salt bridge mutations in the M3 domain also impairs the refolding probability of both M1 and M3 at lower forces during force-decrease scans. These observations suggest that the salt bridges between M1 and M3 play a crucial role in directing the refolding pathways for both subdomains.

Importantly, our results revealed a stark contrast in mechanical stability between the HMP-2/HMP-1 interface and the mammalian α-catenin/β-catenin counterpart. At a constant force of approximately 12 pN, the lifetime of the HMP-2/HMP-1 interface is around 100 s, whereas the α-catenin/β-catenin interface lasts less than one second (11). In addition, comparison between Fig. 5*D* and Fig. 2*D* reveals that the HMP-2/HMP-1 interface disrupts at forces higher than those required to unfold the M1 and M3 subdomains at the same loading rate. This indicates that this force-bearing interface provides sufficient mechanical stability to activate HMP-1's M domain. Along with the higher mechanical stability of HMP-1's M domain compared to mouse/human α-catenin's M domain, the results suggest that this critical mechanosensing force-transmission linkage in *C. elegans* has evolved to operate at a higher activating force threshold.

Furthermore, we have shown that the mechanical stability of the HMP-2/HMP-1 interface is compromised by single phosphomimetic mutations (Y69E and S47E) in HMP-2. This suggests a destabilization of the tension-transmission supramolecular linkage and, consequently, a suppression of the activation of the modulation domains for their respective interactors. These results indicate a complex interplay between mechanical and biochemical regulation of HMP-2/HMP-1-mediated mechanosensing at cell–cell adhesions in *C. elegans*, which aligns with previous observations that phosphomimetic mutations in HMP-2 lead to the disruption of adherens junctions in vivo (20). The enhanced stability of the HMP-2/HMP-1 interface and the increased force required to release the autoinhibited M1 domain raise an intriguing question: Do *C. elegans* cells experience higher intercellular tension compared to mammalian cells? This would necessitate a more robust force-transmission pathway and a higher force-activation threshold for the binding of force-dependent interacting proteins. Testing this possibility awaits additional experiments in situ.

Another intriguing question arises concerning the molecular mechanisms that confer high mechanical stability to the HMP-2/HMP-1 interface. The structure of the HMP-2/HMP-1 interface reveals that it forms through interactions between a single α-helix from the N terminus of HMP-2 and the N-terminal 4-α-helical bundle (N1 domain) of HMP-1, resulting in a 5-α-helical bundle in the complex (19). Actomyosin contraction generates tensile forces in the tension-transmission linkage. As a result, the HMP-2/HMP-1 interface is subject to shear force, i.e., the applied force is nearly parallel to the interacting interface. This arrangement of protein–protein interfaces and the force-pulling geometry is also found in several other crucial force-bearing interfaces, such as vinculin-talin, vinculin-α-catenin, and β-catenin-α-catenin. These interfaces are located in different tension-transmission supramolecular linkages, playing essential roles in mechanotransduction at focal adhesions and cell–cell adhesions (1).

Collectively, these findings suggest that protein–protein interfaces formed between a peptide and a rigid structural domain, under shear-force pulling geometry, could represent an evolutionarily conserved key mechanism for providing high mechanical stability to tension-bearing interfaces (1).

While our study offers insights into the force transmission and mechanotransduction mediated by the HMP-2/HMP-1 complex in *C. elegans*, several limitations need to be addressed in future studies to further understand the physiological relevance of these findings. We have shown that the VBS in HMP-1's M1 subdomain strictly requires mechanical unfolding to be exposed. However, since the functional role of DEB-1/vinculin in *C. elegans* is not fully understood, the physiological significance of this finding has yet to be investigated. To fully comprehend the mechanical stability of this force-transmission linkage, it is necessary to quantify not only the HMP-2/HMP-1 interface but also the mechanical stability of the HMR-1 homodimer at the adherens junction, the HMR-1/HMP-2 interface, and the HMP-1/F-actin interface. Additionally, the impact of site-specific phosphorylation on the mechanical stability of the HMP-2/HMP-1 interface should be investigated further using more physiologically relevant, kinase-dependent phosphorylation approaches. Furthermore, SRGP-1, an important GTPase-activating protein known to interact with HMP-1's M domain (37), requires future studies to understand how force quantitatively affects this critical binding. Finally, a conformational change in HMP-1 was previously hypothesized to promote recruitment of AFD-1/afadin to sites of increased tension during embryonic morphogenesis in the *C. elegans* embryo (43), which warrants future studies.

Materials and Methods

Plasmid Constructs and Protein Expression. Seven plasmids were prepared for expression of the protein constructs for single-molecule stretching experiments: 1) pET151-Avi-(I27)$_2$-(full-length HMP-1)-(I27)$_2$-Spy, 2) pET151-Avi-(I27)$_2$-(HMP-1-M123)-(I27)$_2$-Spy, 3) pET151-Avi-(I27)$_2$-(HMP-1-M1)-(I27)$_2$-Spy, 4) pET151-Avi-(I27)$_2$-(HMP-1-M123-M3$^{R551A,\ R554A}$)-(I27)$_2$-Spy, 5) pET151-Avi-(I27)$_2$-(HMP-1-N12)-(long flexible linker)-(HMP-2-Nt)-(I27)$_2$-Spy, 6) pET151-Avi-(I27)$_2$-(HMP-1-N12)-(long flexible linker)-(HMP-2-Nt^{Y69E})-(I27)$_2$-Spy, 7) pET151-Avi-(I27)$_2$-(HMP-1-N12)-(long flexible linker)-(HMP-2-Nt^{S47E})-(I27)$_2$-Spy. Briefly, the DNA fragments encoding HMP-1 domains were amplified by Polymerase Chain Reaction (PCR) from the template sequences (19, 20). The long flexible linker and other DNA fragments were synthesized by geneArt/IDTgblock. The DNA fragments were then assembled into a pET151-avi-(I27)$_2$-(inset)-(I27)$_2$-spy plasmid template (27) by HiFi DNA Assembly (NEB) and sequencing-confirmed (first BASE). Each plasmid was co-transformed with a BirA plasmid and expressed in *Escherichia coli* BL21 (DE3) cultured in LB-media with D-Biotin (Sigma Aldrich), and affinity purified through the 6X His-tag. Detailed sequence information of the plasmids can be found in *SI Appendix*, Text S1.

Single-Protein Manipulation and Analysis. A vertical magnetic tweezers setup was combined with a disturbance-free, rapid solution-exchange flow channel for conducting in vitro protein stretching experiments (23–25). All in vitro protein stretching experiments were performed in solution containing: 1X Phosphate-buffered saline (PBS), 1% Bovine Serum Albumin (BSA), 2 mM Dithiothreitol (DTT), 10 mM sodium L-ascorbate at 22 ± 1 °C. The force calibration of the magnetic tweezers setup has a 10% uncertainty due to the heterogeneity of the diameter of paramagnetic beads (23) and the bead height determination of the magnetic tweezers setup has a ∼2 to 5 nm uncertainty due to the thermal fluctuation of the tethered bead and the resolution of the camera (10).

Data, Materials, and Software Availability. All study data are included in the article and/or *SI Appendix*.

ACKNOWLEDGMENTS. We thank the protein expression core and science communication core of the Mechanobiology Institute. This research is supported by National Research Foundation (NRF) Singapore, Mechanobiology Institute under its MID-SIZED GRANT (MSG) (NRF-MSG-2023-0001 to J.Y.), the Singapore Ministry of Education Academic Research Funds Tier 2 (MOE-T2EP50123-0008 to J.Y.), the National Natural Science Foundation of China (NSFC Grant NO.32271367 and 12204389 to S.L., NO.32301094 to M.Y.), and the Institute of General Medical Sciences, NIH (R01 GM058038 and R35 GM145312 to J.H.).

Author affiliations: [a]Mechanobiology Institute, National University of Singapore, Singapore 117411, Singapore; [b]Department of Physics, Xiamen University, Xiamen 361000, China; [c]Department of Biochemistry and Division of Orthopaedic Surgery of the Second Affiliated Hospital,, Zhejiang University, Hangzhou 310058, China; [d]Department of Physics, National University of Singapore, Singapore 117542, Singapore; [e]Department of Integrative Biology, University of Wisconsin-Madison, Madison, WI 53706; [f]Biophysics Program, University of Wisconsin-Madison, Madison, WI 53706; [g]Centre for Bioimaging Sciences, National University of Singapore, Singapore 117557, Singapore; and [h]Joint School of National University of Singapore and Tianjin University, International Campus of Tianjin University, Binhai New City, Fuzhou 350207, China

1. S. Le, M. Yu, J. Yan, Mechanical regulation of tension-transmission supramolecular linkages. *Curr. Opin. Solid State Mater. Sci.* **25**, 100895 (2021).
2. N. Borghi *et al*., E-cadherin is under constitutive actomyosin-generated tension that is increased at cell-cell contacts upon externally applied stretch. *Proc. Natl. Acad. Sci. U.S.A.* **109**, 12568–12573 (2012).
3. G. Charras, A. S. Yap, Tensile forces and mechanotransduction at cell–cell junctions. *Curr. Biol.* **28**, R445–R457 (2018).
4. Y. Hirano, Y. Amano, S. Yonemura, T. Hakoshima, The force-sensing device region of α-catenin is an intrinsically disordered segment in the absence of intramolecular stabilization of the autoinhibitory form. *Genes Cells* **23**, 370–385 (2018).
5. M. Yao *et al*., Force-dependent conformational switch of α-catenin controls vinculin binding. *Nat. Commun.* **5**, 4525 (2014).
6. C. D. Buckley *et al*., Cell adhesion. The minimal cadherin-catenin complex binds to actin filaments under force. *Science* **346**, 1254211 (2014).
7. D. L. Huang, N. A. Bax, C. D. Buckley, W. I. Weis, A. R. Dunn, Vinculin forms a directionally asymmetric catch bond with F-actin. *Science* **357**, 703–706 (2017).
8. B. Ladoux, R. M. Mège, Mechanobiology of collective cell behaviours. *Nat. Rev. Mol. Cell Biol.* **18**, 743–757 (2017).
9. S. Barrick *et al*., Salt bridges gate α-catenin activation at intercellular junctions. *Mol. biol. cell* **29**, 111–122 (2018).
10. S. Le, M. Yu, J. Yan, Phosphorylation reduces the mechanical stability of the α-catenin/ β-catenin complex. *Angew. Chem. Int. Ed. Engl.* **58**, 18663–18669 (2019).
11. S. Le, M. Yu, J. Yan, Direct single-molecule quantification reveals unexpectedly high mechanical stability of vinculin-talin-α-catenin linkages. *Sci. Adv.* **5**, eaav2720 (2019).
12. S. M. Pang, S. Le, A. V. Kwiatkowski, J. Yan, Mechanical stability of αT-catenin and its activation by force for vinculin binding. *Mol. Biol. Cell* **30**, 1930–1937 (2019).
13. S. Pokutta, W. I. Weis, Structure of the dimerization and β-catenin-binding region of α-catenin. *Mol. Cell* **5**, 533–543 (2000).
14. J. S. Simske *et al*., The cell junction protein VAB-9 regulates adhesion and epidermal morphology in *C. elegans*. *Nat. Cell Biol.* **5**, 619–625 (2003).
15. E. A. Cox, J. Hardin, Sticky worms: Adhesion complexes in *C. elegans*. *J. Cell Sci.* **117**, 1885–1897 (2004).
16. L. J. Neukomm *et al*., Loss of the RhoGAP SRGP-1 promotes the clearance of dead and injured cells in *Caenorhabditis elegans*. *Nat. Cell Biol.* **13**, 79–86 (2011).
17. R. Zaidel-Bar *et al*., The F-bar domain of SRGP-1 facilitates cell-cell adhesion during *C. elegans* morphogenesis. *J. Cell Biol.* **191**, 761–769 (2010).
18. J. Hardin, A. Lynch, T. Loveless, J. Pettitt, Cadherins and their partners in the nematode worm *Caenorhabditis elegans*. *Prog. Mol. Biol. Transl. Sci.* **116**, 239–262 (2013).
19. H. Kang *et al*., Structural and functional characterization of *Caenorhabditis elegans* α-catenin reveals constitutive binding to β-catenin and F-actin. *J. Biol. Chem.* **292**, 7077–7086 (2017).
20. X. Shao *et al*., Cell-cell adhesion in metazoans relies on evolutionarily conserved features of the α-catenin·β-catenin-binding interface. *J. Biol. Chem.* **292**, 16477–16490 (2017).
21. X. Shao, B. Lucas, J. Strauch, J. Hardin, The adhesion modulation domain of *Caenorhabditis elegans* α-catenin regulates actin binding during morphogenesis. *Mol. Biol. Cell* **30**, 2115–2123 (2019).
22. T. T. K. Vuong-Brender, A. Boutillon, D. Rodriguez, V. Lavilley, M. Labouesse, HMP-1/α-catenin promotes junctional mechanical integrity during morphogenesis. *PLoS One* **13**, e0193279 (2018).
23. H. Chen *et al*., Improved high-force magnetic tweezers for stretching and refolding of proteins and short DNA. *Biophys. J.* **100**, 517–523 (2011).
24. S. Le *et al*., Disturbance-free rapid solution exchange for magnetic tweezers single-molecule studies. *Nucleic Acids Res.* **43**, e113–e113 (2015).
25. S. Le, R. Liu, C. T. Lim, J. Yan, Uncovering mechanosensing mechanisms at the single protein level using magnetic tweezers. *Methods* **94**, 13–18 (2016).
26. G. Yuan *et al*., Elasticity of the transition state leading to an unexpected mechanical stabilization of titin immunoglobulin domains. *Angew. Chem. Int. Ed. Engl.* **56**, 5490–5493 (2017).
27. S. Le *et al*., Mechanotransmission and mechanosensing of human α-actinin 1. *Cell Rep.* **21**, 2714–2723 (2017).
28. S. Le *et al*., Dystrophin as a molecular shock absorber. *ACS Nano* **12**, 12140–12148 (2018).
29. B. Zakeri *et al*., Peptide tag forming a rapid covalent bond to a protein, through engineering a bacterial adhesin. *Proc. Natl. Acad. Sci. U.S.A.* **109**, E690–E697 (2012).
30. S. Le *et al*., Mechanical force antagonizes the inhibitory effects of RecX on RecA filament formation in mycobacterium tuberculosis. *Nucleic Acids Res.* **42**, 11992–11999 (2014).
31. X. Zhao, X. Zeng, C. Lu, J. Yan, Studying the mechanical responses of proteins using magnetic tweezers. *Nanotechnology* **28**, 414002 (2017).
32. M. Yu, J. H. Lu, S. Le, J. Yan, Unexpected low mechanical stability of titin I27 domain at physiologically relevant temperature. *J. Phys. Chem. Lett.* **12**, 7914–7920 (2021).
33. H. J. Choi *et al*., αE-catenin is an autoinhibited molecule that coactivates vinculin. *Proc. Natl. Acad. Sci. U.S.A.* **109**, 8576–8581 (2012).
34. D. Spadaro *et al*., Tension-dependent stretching activates ZO-1 to control the junctional localization of its interactors. *Curr. Biol.* **27**, 3783–3795.e8 (2017).
35. M. Yu *et al*., Force-dependent regulation of talin-KANK1 complex at focal adhesions. *Nano Lett.* **19**, 5982–5990 (2019).
36. Y. Wang *et al*., Label-free single-molecule quantification of rapamycin-induced FKBP-FRB dimerization for direct control of cellular mechanotransduction. *Nano Lett.* **19**, 7514–7525 (2019).
37. J. M. Serre *et al*., *C. elegans* srGAP is an *alpha*-catenin m domain-binding protein that strengthens cadherin-dependent adhesion during morphogenesis. *Development* **149**, dev200775 (2022).
38. N. Ishiyama *et al*., An autoinhibited structure of α-catenin and its implications for vinculin recruitment to adherens junctions. *J. Biol. Chem.* **288**, 15913–15925 (2013).
39. J. Li *et al*., Structural determinants of the mechanical stability of α-catenin. *J. Biol. Chem.* **290**, 18890–18903 (2015).
40. M. Yao *et al*., The mechanical response of talin. *Nat. Commun.* **7**, 11966 (2016).
41. Y. Hu *et al*., DNA-based forcechrono probes for deciphering single-molecule force dynamics in living cells. *Cell* **187**, 3445–3459 (2024).
42. M. H. Jo *et al*., Determination of single-molecule loading rate during mechanotransduction in cell adhesion. *Science* **383**, 1374–1379 (2024).
43. J. M. Serre, M. M. Slabodnick, B. Goldstein, J. Hardin, RGP-1/srGAP and AFD-1/afadin stabilize HMP-1/*alpha*-catenin at rosettes to seal internalization sites following gastrulation in *C. elegans*. *PLoS genet.* **19**, e1010507 (2023).

Supporting Information for

Single-molecule force spectroscopy reveals intra- and intermolecular interactions of *C. elegans* HMP-1 during mechanotransduction

Shimin Le, Miao Yu, Chaoyu Fu, Jonathon A. Heier, Sterling Martin, Jeff Hardin and Jie Yan

Jie Yan.
E-mail: J.Y.: phyyj@nus.edu.sg

This PDF file includes:

Supporting text
Figs. S1 to S8
Tables S1 to S2
SI References

Supporting Information Text

Supplementary Text S1. Plasmids construct and protein expression. Seven plasmids were prepared for expression of the protein constructs for single-molecule stretching experiments: 1). pET151-Avi-$(I27)_2$-(full length HMP-1)-$(I27)_2$-Spy, 2) pET151-Avi-$(I27)_2$-(HMP-1-M123)-$(I27)_2$-Spy, 3) pET151-Avi-$(I27)_2$-(HMP-1-M1)-$(I27)_2$-Spy, 4). pET151-Avi-$(I27)_2$-(HMP-1-M123-M3$^{R551A,\ R554A}$)-$(I27)_2$-Spy, 5). pET151-Avi-$(I27)_2$-(HMP-1-N12)-(long flexible linker)-(HMP-2-Nt)-$(I27)_2$-Spy, 6). pET151-Avi-$(I27)_2$-(HMP-1-N12)-(long flexible linker)-(HMP-2-Nt^{Y69E})-$(I27)_2$-Spy, 7). pET151-Avi-$(I27)_2$-(HMP-1-N12)-(long flexible linker)-(HMP-2-Nt^{S47E})-$(I27)_2$-Spy. Briefly, the DNA fragments encoding HMP-1 domains were amplified by PCR the template sequence (1, 2). The long flexible linker and other DNA fragments were synthesized by geneArt/IDTgblock. The DNA fragments were then assembled into a pET151-avi-$(I27)_2$-(inset)-$(I27)_2$-spy plasmid template (3) by HiFi DNA Assembly (NEB) and sequencing-confirmed (1st BASE). Each plasmid was co-transformed with a BirA plasmid and expressed in *Escherichia coli* BL21 (DE3) cultured in LB-media with D-Biotin (Sigma Aldrich), and affinity purified through 6His-tag (at N-terminus). Detailed sequence information of the plasmids are listed below:

1). Avi-$(I27)_2$-(full length HMP-1)-$(I27)_2$-Spy:

HHHHHHGKPIPNPLLGLDSTENLYFQGIDPFTGLNDIFEAQKIEWHEGGGSGLIEVEKPLYGVEVFVGETAHFEIELSEPDVHGQWKLKGQPLAASPDAEIIEDGKKHILILHNAQLGMTGEVSFQAANTKSAANLKVKELGGGSGLIEVEKPLYGVEVFVGETAHFEIELSEPDVHGQWKLKGQPLAASPDAEIIEDGKKHILILHNAQLGMTGEVSFQAANTKSAANLKVKELGGGSGKLMPANGNSHAYFNIDEVRSKNVLKQITQLINEVTNITETFPLKPGQTTEGLVATLDAAVANFLQTGSFAISKCPIANSDPRAIDLLHEALGAVQDTGQVMIQTGRDFVRDSTSTNKRAIATNSGRNLLTAVAKFLILADSIDVKVIVDKVDEVRETAHQMIEADTKIKVDDLYNLLISQIEELDITVRRRAIDLVKPNQRDDLLAARSALRQTAPLLYTSTRTFVRHPEHEEARRNRDYTADEMHSALNALESVLNGQQPKVTFSEYGRIGDLINEIDTFQNRIEIDPAHYRRGTDRPDLEGHCERIVSGSASIADAESTRENRKQKIVAECNNLRQALQELLTEYEKSTGRRDDNDDIPLGIAEVHKRTKDLRRHLRRAIVDHISDAFLDTRTPLILLIEAAKEGHEENTRYRSKMFQEHANEIVSVARLSCQLSSDVESVSVIQHTAAQLEKLAPQVAQAAILLCHQPTSKTAQENMETYKNAWFDKVRLLTTALDNITTLDDFLAVSEAHIVEDCERGIKGITANASTPDENAANCETVDCAAGSIRGRALRVCDVVDAEMDFLQNSEYTETVKQAVRILKTQRVDQFAERASALANRQEAHGLTWDPKTKEEEMNEFINACTLVHDAVKDIRHALLMNRSMNDVDSDVEYEADGVGAANADANRTISEQENQQNLMRRLPEEEKKKIQAQIDIFKVTQTRFEREVAKWDETGNDIISLANNMCKIMMSMTEFTRGCGPLKTTMDVIRAAQEISLNGSKLNALARQIGEESADSQTKKDLLAYLSQITLYCQQLNICSKVKADVTQVGNELVVSALDSAMSLIQTARNLLTAVVQTVKAAYIASTKFRRPNANSVRVEWRMAPPKKQPLIRPQKNNAIIRRASERRPLQPAKVLAEFTRNEIETGRDSDDEELDRRHQQRINGRLLEGGGSGLIEVEKPLYGVEVFVGETAHFEIELSEPDVHGQWKLKGQPLAASPDAEIIEDGKKHILILHNAQLGMTGEVSFQAANTKSAANLKVKELGGGSGLIEVEKPLYGVEVFVGETAHFEIELSEPDVHGQWKLKGQPLAASPDAEIIEDGKKHILILHNAQLGMTGEVSFQAANTKSAANLKVKELGGGSGAHIVMVDAYKPTK *

2). Avi-$(I27)_2$-(HMP-1-M123)-$(I27)_2$-Spy:

HHHHHHGKPIPNPLLGLDSTENLYFQGIDPFTGLNDIFEAQKIEWHEGGGSGLIEVEKPLYGVEVFVGETAHFEIELSEPDVHGQWKLKGQPLAASPDAEIIEDGKKHILILHNAQLGMTGEVSFQAANTKSAANLKVKELGGGSGLIEVEKPLYGVEVFVGETAHFEIELSEPDVHGQWKLKGQPLAASPDAEIIEDGKKHILILHNAQLGMTGEVSFQAANTKSAANLKVKELGGGSGKLGQQPKVTFSEYGRIGDLINEIDTFQNRIEIDPAHYRRGTDRPDLEGHCERIVSGSASIADAESTRENRKQKIVAECNNLRQALQELLTEYEKSTGRRDDNDDIPLGIAEVHKRTKDLRRHLRRAIVDHISDAFLDTRTPLILLIEAAKEGHEENTRYRSKMFQEHANEIVSVARLSCQLSSDVESVSVIQHTAAQLEKLAPQVAQAAILLCHQPTSKTAQENMETYKNAWFDKVRLLTTALDNITTLDDFLAVSEAHIVEDCERGIKGITANASTPDENAANCETVDCAAGSIRGRALRVCDVVDAEMDFLQNSEYTETVKQAVRILKTQRVDQFAERASALANRQEAHGLTWDPKTKEEEMNEFINACTLVHDAVKDIRHALLMNRSMNDVDSDVEYEADGVGAANADANRTISEQLEGGGSGLIEVEKPLYGVEVFVGETAHFEIELSEPDVHGQWKLKGQPLAASPDAEIIEDGKKHILILHNAQLGMTGEVSFQAANTKSAANLKVKELGGGSGLIEVEKPLYGVEVFVGETAHFEIELSEPDVHGQWKLKGQPLAASPDAEIIEDGKKHILILHNAQLGMTGEVSFQAANTKSAANLKVKELGGGSGAHIVMVDAYKPTK *

3). Avi-$(I27)_2$-(HMP-1-M1)-$(I27)_2$-Spy:

HHHHHHGKPIPNPLLGLDSTENLYFQGIDPFTGLNDIFEAQKIEWHEGGGSGLIEVEKPLYGVEVFVGETAHFEIELSEPDVHGQWKLKGQPLAASPDAEIIEDGKKHILILHNAQLGMTGEVSFQAANTKSAANLKVKELGGGSGLIEVEKPLYGVEVFVGETAHFEIELSEPDVHGQWKLKGQPLAASPDAEIIEDGKKHILILHNAQLGMTGEVSFQAANTKSAANLKVKELGGGSGKLGQQPKVTFSEYGRIGDLINEIDTFQNRIEIDPAHYRRGTDRPDLEGHCERIVSGSASIADAESTRENRKQKIVAECNNLRQALQELLTEYEKSTGRRDDNDDIPLGIAEVHKRTKDLRRHLRRAILEGGGSGLIEVEKPLYGVEVFVGETAHFEIELSEPDVHGQWKLKGQPLAASPDAEIIEDGKKHILILHNAQLGMTGEVSFQAANTKSAANLKVKELGGGSGLIEVEKPLYGVEVFVGETAHFEIELSEPDVHGQWKLKGQPLAASPDAEIIEDGKKHILILHNAQLGMTGEVSFQAANTKSAANLKVKELGGGSGAHIVMVDAYKPTK *

4). Avi-$(I27)_2$-(HMP-1-M123)-$(I27)_2$-Spy: Replace the NCETVDCAAGSIRGRALRVCDVVDAEMDF in 2). to be NCETVDCAAGSIRGAALAVCDVVDAEMDF.

5). Avi-$(I27)_2$-(HMP-1-N12)-Long Linker-(HMP-2-Nt)-$(I27)_2$-Spy:

HHHHHHGKPIPNPLLGLDSTENLYFQGIDPFTGLNDIFEAQKIEWHEGGGSGLIEVEKPLYGVEVFVGETAHFEIELSEPDVHGQWKLKGQPLAASPDAEIIEDGKKHILILHNAQLGMTGEVSFQAANTKSAANLKVKELGGGSGLIEVEKPLYGVEVFVGETAHFEIELSEPDVHGQWKLKGQPLAASPDAEIIEDGKKHILILHNAQLGMTGEVSFQAANTKSAANLKVKELGGGSGKLMPANGNSHAYFNIDEVRSKNVLKQITQLINEVTNITETFPLKPGQTTEGLVATLDAAVANFLQTGSFAISKCPIANSDPRAIDLLHEALGAVQDTGQVMIQTGRDFVRDSTSTNKRAIATNSGRNLLTAVAKFLILADSIDV

KVIVDKVDEVRETAHQMIEADTKIKVDDLYNLLISQIEELDITVRRRAIDLVKPNQRDDLLAARSALRQTAPLLYTSTRTFVRHPEHEEARRNRDYTADEMHSALNALESVLNGGGSGLKGGGSGVPGGEKKVRKLLPERKPEPKEEVVLKSVLRKRPEEEEPKVEPKKPKPEAEVKTIKPPPVEPEPTPIAAPVTVPVVGKKAEAKAPKEEAAKPKGPIKGVPKKTPSPIEAERRKLRPGSGGEKPPDEASSSPPGSGGGSGGGGSGKLGDIEFIKVNKGGGGSGGGGSGTSAAEATNSTTSIVEMMQMPTQQLKQSVMDLLTYEGSNDMSGLSGGGSGGGGSLEGGGSGLIEVEKPLYGVEVFVGETAHFEIELSEPDVHGQWKLKGQPLAASPDAEIIEDGKKHILILHNAQLGMTGEVSFQAANTKSAANLKVKELGGGSGLIEVEKPLYGVEVFVGETAHFEIELSEPDVHGQWKLKGQPLAASPDAEIIEDGKKHILILHNAQLGMTGEVSFQAANTKSAANLKVKELGGGSGAHIVMVDAYKPTK *

6). Avi-(I27)$_2$-(HMP-1-N12)-Long Linker-(HMP-2-Nt$^{\mathrm{Y69E}}$)-(I27)$_2$-Spy: Replace the TSAAEATNSTTSIVEMMQMPTQQLKQSVMDLLTYEGSNDMSGLS in 5). to be TSAAEATNSTTSIVEMMQMPTQQLKQSVMDLLTEEGSNDMSGLS.

7). Avi-(I27)$_2$-(HMP-1-N12)-Long Linker-(HMP-2-Nt$^{\mathrm{S47E}}$)-(I27)$_2$-Spy: Replace the TSAAEATNSTTSIVEMMQMPTQQLKQSVMDLLTYEGSNDMSGLS in 5). to be TSAAEATNSTTEIVEMMQMPTQQLKQSVMDLLTYEGSNDMSGLS.

Supplementary Text S2. Cooperative unfolding. The M1 and M3 domains tend to unfold together at similar forces, suggesting strong cooperativity. Since unfolding occurs during a pulling process with a loading rate of 1 pN/s, the difference in unfolding forces between the two domains corresponds to the time interval between their unfolding events. Whether these two unfolding events can be distinguished depends on the sampling rate and data smoothing.

Our camera captures bead images at 200 Hz. Consequently, the time resolution for distinguishing separate unfolding events is limited to roughly 0.005 seconds. This translates to approximately 0.005 pN difference in force at a loading rate of 1 pN/s. Due to the thermal noise in extension fluctuations, we detected the stepwise change in bead height for smoothed data after performing a 10-point average of the time trace, which slightly compromised the effective time resolution. Therefore, in our analysis, unfolding events occurring within 0.1 seconds of each other are considered "simultaneous unfolding events." Events separated by a longer time interval are treated as distinct unfolding events. Since the determination is based on a preset time interval threshold, statistics are not involved in this analysis.

Figure S2 shows an example. It shows a zoomed-in view of Figure 2b, which contains five time traces from the same tether, numbered (1) to (5). Time trace (4) is the typical curve that shows simultaneous unfolding, while the rest are treated as distinct unfolding events.

Supplementary Text S3. Evidence of the third unfolding event in M domains aligns with M2 domain unfolding. The force-extension curves of the ruptured adhesion complex and the unfolded peptides of the M domains can be modelled as a worm-like chain (WLC) polymer using the Marko-Siggia formula (4), Equation 1: $\frac{fA}{k_BT} = \frac{1}{4(1-x(f)/L)^2} + \frac{x(f)}{L} - \frac{1}{4}$

Here, k_BT is a constant related to thermal energy, L represents the contour length of the polymer, and A is the persistence length. For the known unfolding force f and unfolding step size x(f) of M domains, the unfolding contour length of M domains can be calculated based on the Equation 1. The persistence length of M domains can be estimated as 0.8 (5, 6). The contour length was further converted to the number of amino acids (approximately 0.38 nm per amino acid) (7).

Table S1. Contour length of M subdomains.

M domains	Number of amino acids (a.a.)	Contour length (nm)
M1	120a.a.	45.6nm
M2	111a.a.	42.2nm
M3	146a.a.	55.5nm

Based on the unfolding force of the third unfolding event in the M domain (17.8±1.5 pN) and the unfolding step size of the third unfolding event in the M domain (28.1±4.8 nm), the released contour length of the third unfolding event in the M domain can be calculated as 39.5±4.7 nm. This contour length is equivalent to the M2 domain (42.2 nm) and is much smaller than the contour length of the M3 domain (55.5 nm), which supports the conclusion that the third unfolding event aligns with M2 domain unfolding.

Supplementary Text S4. Physiologically relevant force range. The orientation of force-bearing structural domains (primarily the N2 domain and the M domains) along with the flexible polypeptide linkers occur at a force on the order of 1 pN. This can be estimated based on $k_\mathrm{B}T/b$, where $k_\mathrm{B}T \approx 4.1$ pN·nm is the thermal energy, and b is the size of a structural domain or the bending persistence length of a polypeptide chain, which is typically on the order of a few nm. In addition, as quantified in the study, the unfolding of the M domains occurs at forces less than 20 pN at physiologically relevant force loading rates of a few pN/s. Consequently, the force is effectively buffered within 20 pN when the force-bearing linkage extends up to 150 nm (considering the orientation of the domains toward the stretching direction and unfolding of each domain causes extension by roughly 30 nm). Moreover, as illustrated in Figure 5f, the HMP1/HMP2 interface dissociates over a sub-second timescale when forces exceed 20 pN. Therefore, the forces exerted on a single HMP1/HMP2-mediated force-transmission linkage are consistently buffered within 20 pN. Thus, forces significantly exceeding 20 pN are not physiologically relevant.

Supplementary Text S5. Summary of mechanical properties of HMP-1 modulation domains and HMP-1-HMP-2 interface with relevant mutants. Below is a summary table of mechanical properties of HMP-1 modulation domains and HMP-1-HMP-2 interface with relevant mutants at a loading rate of 1pN s^{-1}.

Table S2

<table>
<tr><th colspan="3">HMP-1 modulation domains (Unfolding force)</th></tr>
<tr><td>M domains</td><td>Wild type</td><td>Salt bridge mutants</td></tr>
<tr><td>M1</td><td>∼13 pN</td><td>8.3 pN</td></tr>
<tr><td>M2</td><td>17.8 pN</td><td>17.9 pN</td></tr>
<tr><td>M3</td><td>∼13 pN</td><td>11.6 pN</td></tr>
<tr><th colspan="3">HMP-1-HMP-2 interface (Rupture force)</th></tr>
<tr><td>Wildtype</td><td>HMP-2^{Y69E}</td><td>HMP-2^{S47E}</td></tr>
<tr><td>16.6 pN</td><td>6.1 pN, 14.1 pN (two steps)</td><td>14.7 pN</td></tr>
</table>

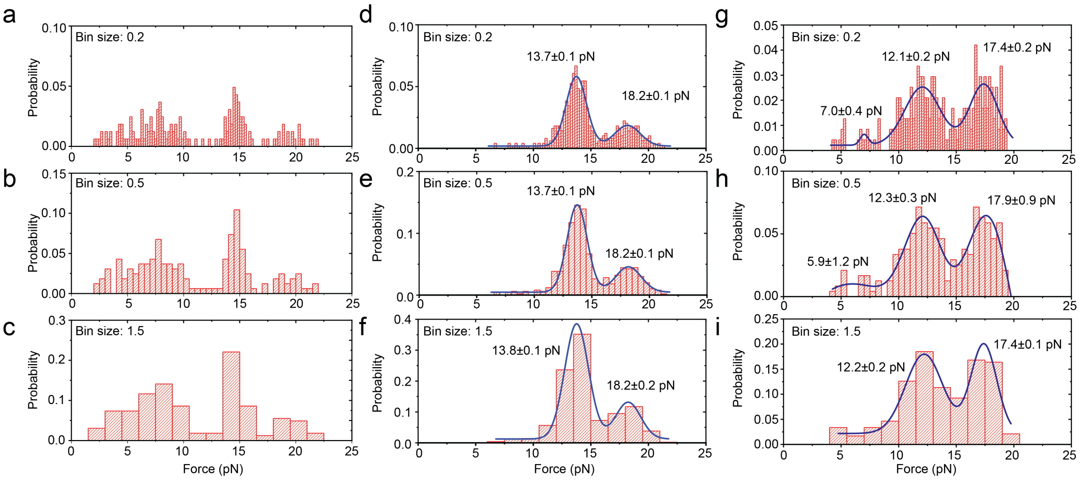

Fig. S1. (a-c). The normalised force histogram from full length HMP-1 obtained with three different bin sizes: 0.2, 0.5 and 1.5. (d-i). The normalised force histogram obtained from modulation domain of HMP-1 (d-f) and after vinculin binding of the modulation domain (g-i) with three different bin sizes: 0.2, 0.5 and 1.5. The double-Gaussian fitting to the normalised unfolding force histogram. The peak forces are indicated.

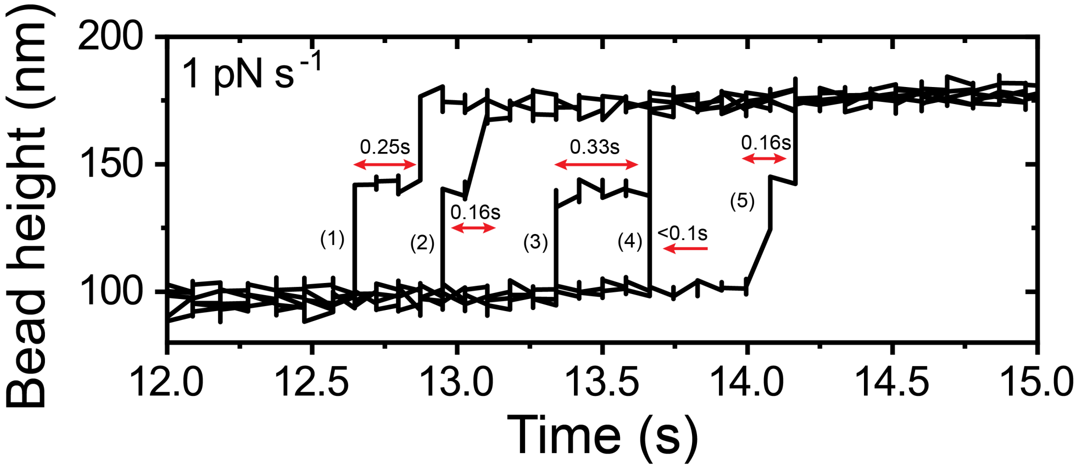

Fig. S2. Five representative force–height curves of the HMP-1 modulation domains during force-increase scans at a loading rate of 1 pN s^{-1}.

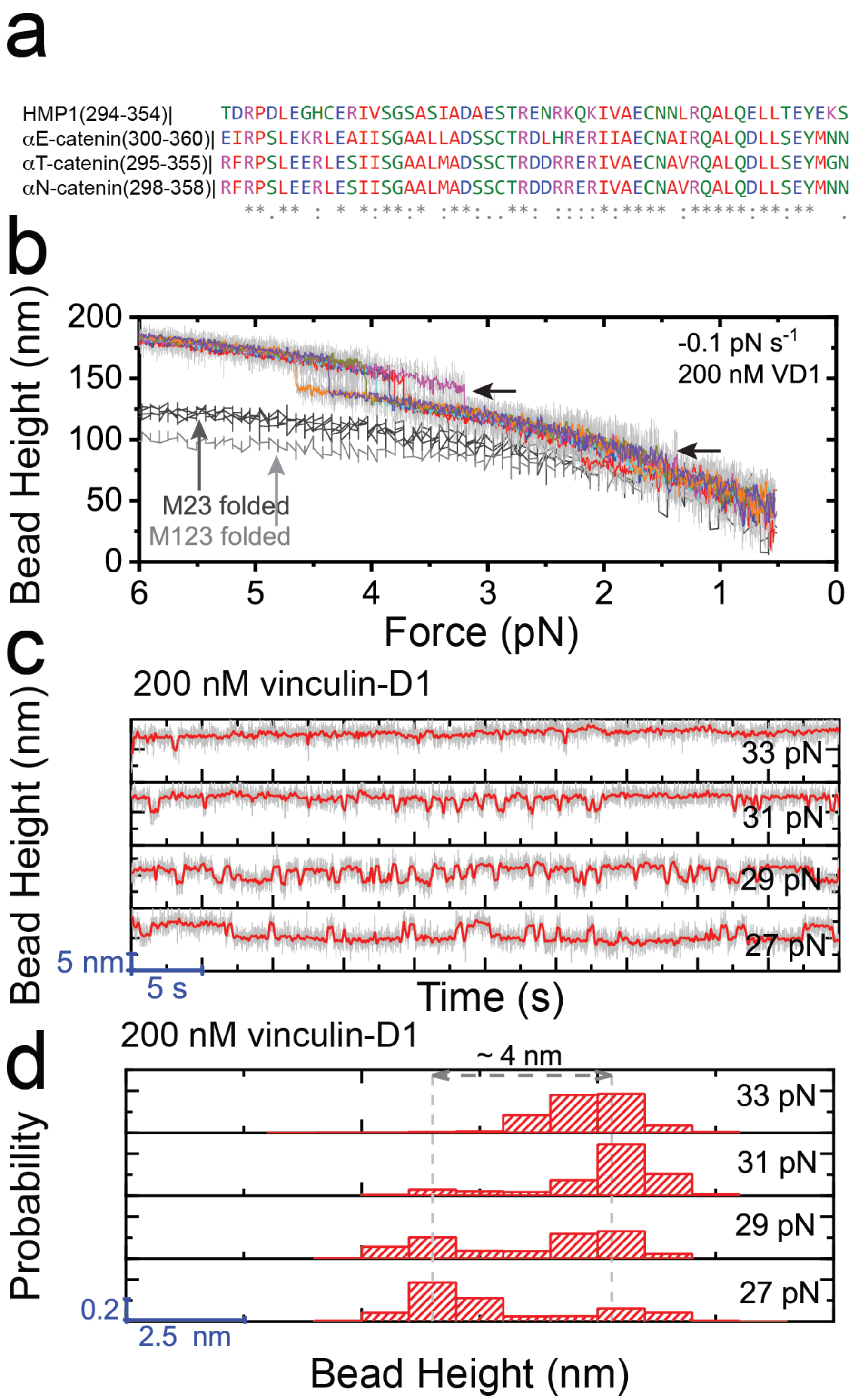

Fig. S3. **Mechanical activation of HMP-1 modulation domains for vinculin-D1 binding.** (a). The sequence alignment of the conserved vinculin binding sites among the HMP-1 and mammalian α-catenins. (b). Eight representative force–height curves (coloured curves) of HMP-1 modulation domains during force-decrease scans with a loading rate of -0.1 pN s^{-1} starting from a fully unfolded conformation in the presence of 200 nM vinculin-D1. As a comparison, the force–height curves of the HMP-1 modulation domains with M123 domains folded (light grey curves) and only M23 domain folded (dark grey curves) are also plotted. (c). Representative force-height curves of the tether at indicated constant forces. Dynamic binding or unbinding events of vinculin-D1 are indicated by 3-5 nm bead height changes, as shown in the resulting normalised histograms of bead height (d).

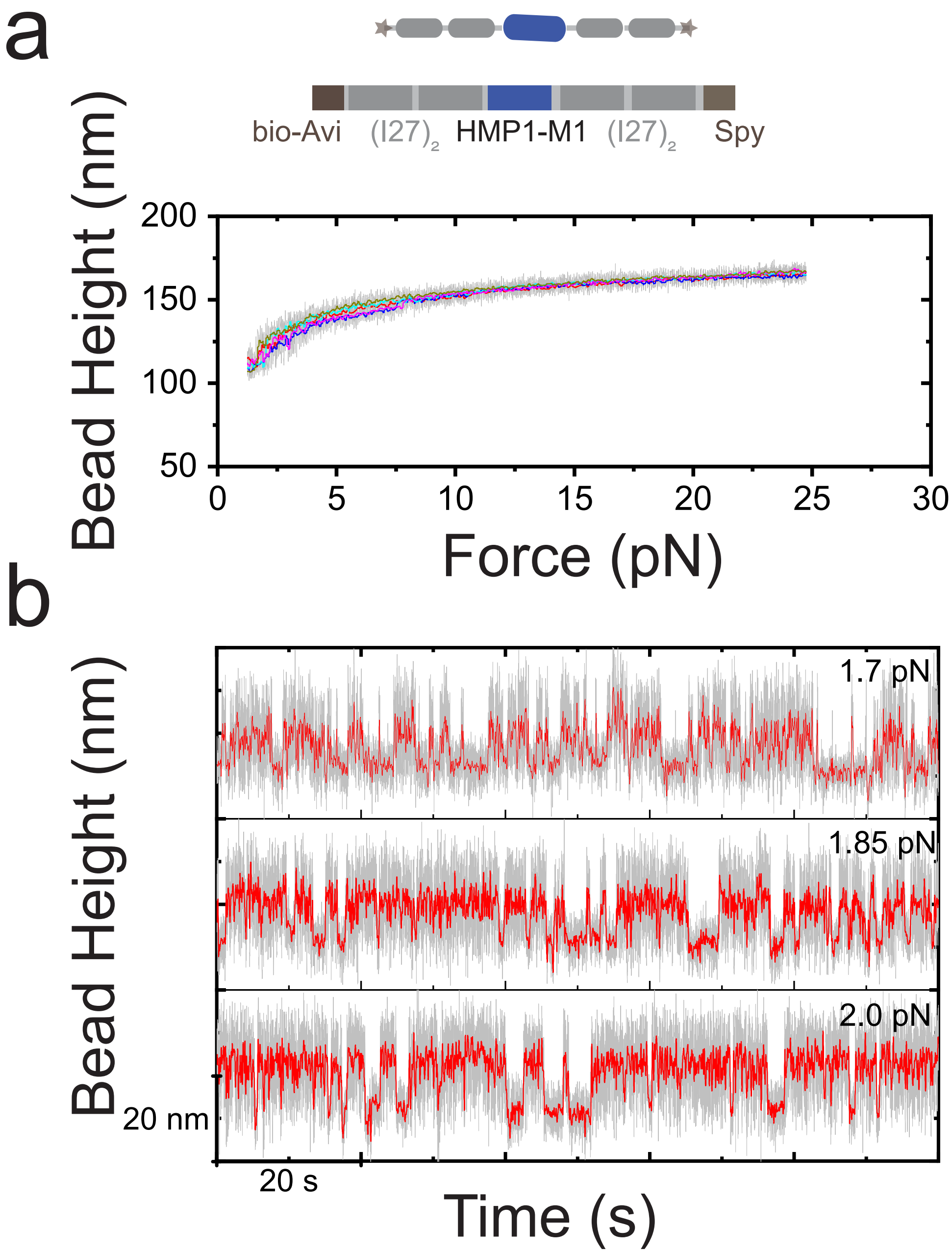

Fig. S4. Force-repsonses of HMP-1 M1 domain. (a). Representative force–bead height curves of the HMP-1 M1 domain at a loading rate of $\sim$ 1 pN s^{-1}. (b). Representative bead height fluctuations of HMP-1 M1 domain at constant forces of $\sim$ 2 pN. Coloured lines are 10-point FFT (Fast Fourier Transform) smoothing of the raw data in grey.

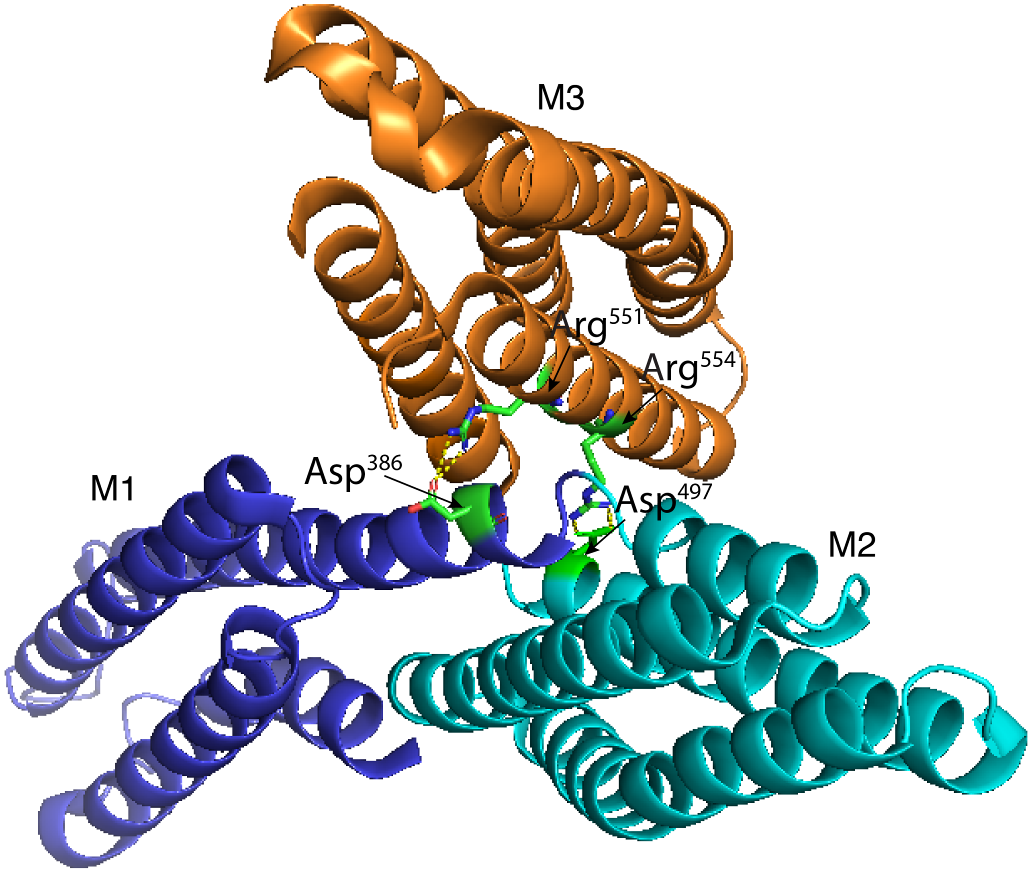

Fig. S5. **Structure of the HMP-1 M domain with salt bridges.** The green amino acids represent the salt bridges between M1, M2 and M3. The Arg^{551} was mutated to Ala^{551} and the Arg^{554} was mutated to Ala^{554} in the salt bridge mutants.

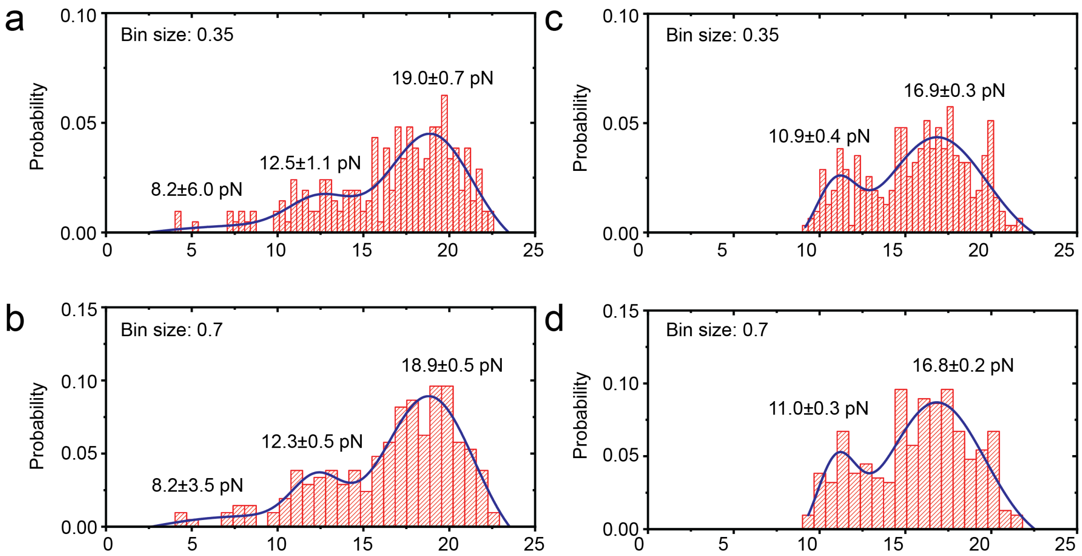

Fig. S6. (a-d). The normalised force histogram obtained from salt bridge mutant of modulation domain of HMP-1 (a-b) and after vinculin binding of the modulation domain (c-d) with three different bin sizes: 0.35 and 0.7. The double-Gaussian fitting to the normalised unfolding force histogram. The peak forces are indicated.

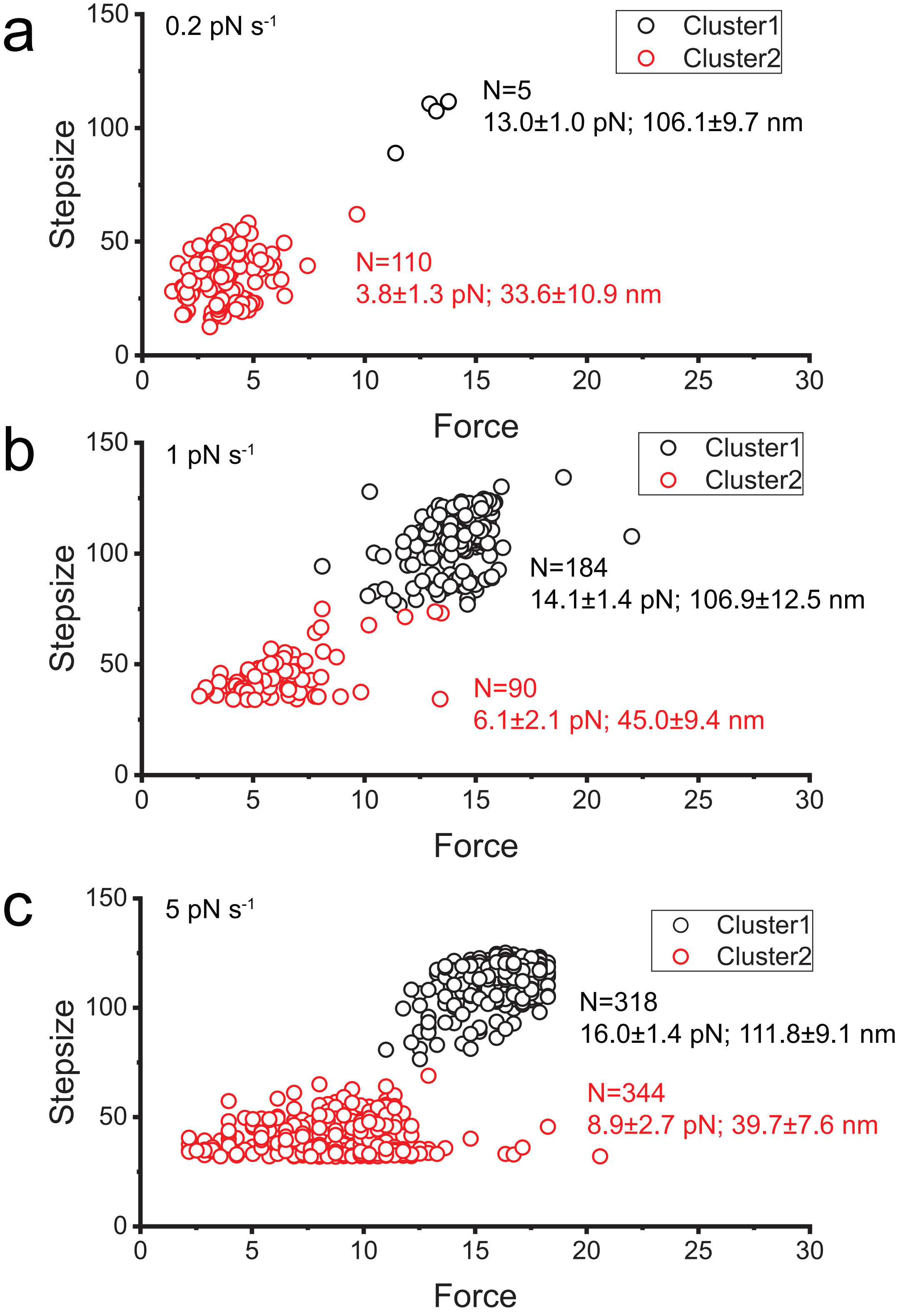

Fig. S7. (a-c). The resulting force-dependent step sizes obtained at the three indicated loading rates: 0.2 pN s^{-1}, 1 pN s^{-1} and 5 pN s^{-1}. The k-mean clustering analysis was performed to identify the two clusters.

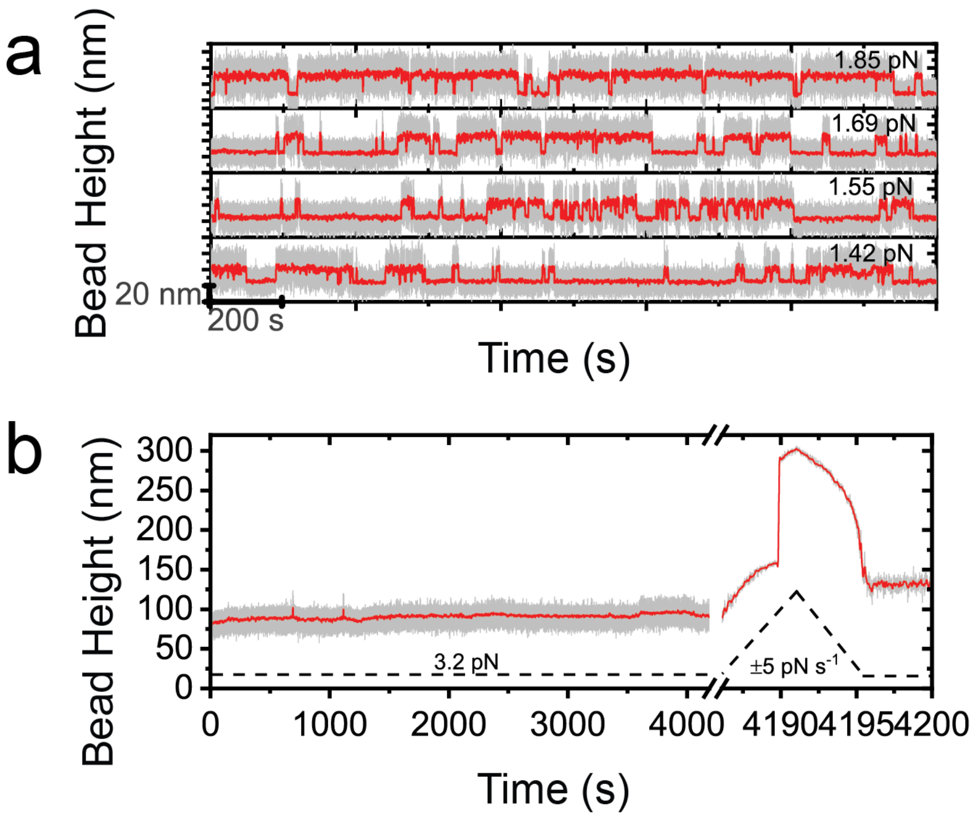

Fig. S8. (a). Representative time traces of the bead height of a HMP-1–HMP-2^{Y69E} interface tether at indicated constant forces, where dynamic formation and rupturing of the interface were observed. (b). Representative time traces of the bead height of a HMP-1–HMP-2^{S47E} tether at a constant force of 3 pN for over 4000 sec where the interface remained stable, followed by a force-increase scan (after the break sign) to rupture the interface.

References

1. H Kang, et al., Structural and functional characterization of caenorhabditis elegans α-catenin reveals constitutive binding to β-catenin and f-actin. *J. Biol. Chem.* **292**, 7077–7086 (2017).
2. X Shao, et al., Cell–cell adhesion in metazoans relies on evolutionarily conserved features of the α-catenin · β-catenin–binding interface. *J. Biol. Chem.* **292**, 16477–16490 (2017).
3. S Le, et al., Mechanotransmission and mechanosensing of human alpha-actinin 1. *Cell reports* **21**, 2714–2723 (2017).
4. C Bustamante, JF Marko, ED Siggia, S Smith, Entropic elasticity of λ-phage dna. *Science* **265**, 1599–1600 (1994).
5. H Chen, et al., Improved high-force magnetic tweezers for stretching and refolding of proteins and short DNA. *Biophys. J.* **100**, 517–523 (2011).
6. M Yao, et al., Force-dependent conformational switch of α-catenin controls vinculin binding. *Nat. communications* **5**, 4525 (2014).
7. RS Winardhi, Q Tang, J Chen, M Yao, J Yan, Probing small molecule binding to unfolded polyprotein based on its elasticity and refolding. *Biophys. journal* **111**, 2349–2357 (2016).